

國立臺灣大學理學院大氣科學研究所

碩士論文

Graduate Institute of Atmospheric Sciences

College of Science

National Taiwan University

Master Thesis



北太平洋副熱帶高壓冬季及冬春轉換的控制因子

The Controlling Factors of the North Pacific Subtropical High

in Winter and Winter-to-Spring Transition

周興泓

Hsing-Hung Chou

指導教授：黃彥婷 博士、林和 博士

Advisors: Yen-Ting Hwang, Ph.D., Ho Lin, Ph.D.

中華民國 111 年 7 月

July 2022

# 國立臺灣大學碩士學位論文 口試委員會審定書

本論文係周興泓君 ( 學號 R09229008 ) 在國立臺灣大學大氣科學學系、所完成之碩士學位論文，於民國 111 年 7 月 19 日承下列考試委員審查通過及口試及格，特此證明

口試委員：

林和

黃育婷

( 簽名 )

( 指導教授 )

陳世偉

梁馬喬

系主任、所長

周興泓

( 簽名 )

## 致謝



待在研究室的時光，默默地也占了台大生活的一半，這段時間要感謝的人太多了，那我就來一一感謝吧。

首先特別感謝我的兩位指導老師：黃彥婷老師和林和老師。謝謝兩位老師總是包容著我的迷惘和鬼打牆。每次跟老師們討論、一起看著新的分析腦力激盪的時候總是覺得特別過癮，也總能感受到滿滿的研究能量，覺得自己在做的事情真的能幫助我們更了解世界一些。希望未來我還能夠帶著這樣的悸動繼續前進。

謝謝 CDGC 的夥伴們，從大三進研究室以來，一路跌跌撞撞到了現在，中間一直讓我覺得做研究很有趣的一大原因，就是實驗室的大家總是樂於討論、互相提供許多想法。正事之餘，那些講幹話和吃好料的時光也讓我覺得有第二個家的感覺，非常的溫馨。

也謝謝 R09 的同學們，每次聽著大家一起互吐苦水，就知道自己在這條艱辛的道路上不孤單。尤其特別感謝系排的同屆們，每個一五放學後的舒壓打球跟吃飯聊天總是有你們在，讓我能夠繼續維持規律運動，保持健康(?)的身體。

最後想要感謝一路支持我的家人們，謝謝你們讓我能無後顧之憂地往前走，知道不管發生什麼事，總是有人會在家聽我傾訴痛苦與快樂。

## 中文摘要



本研究探討北太平洋副熱帶高壓在北半球冬季與冬季轉春季時期的控制因子。我們的分析顯示北太平洋洋盆的西風噴流對於控制副熱帶高壓的強度及位置具有關鍵的作用。其中，噴流強度在緯向上的差異使冬季沉降場有兩個不同的來源：西、中太平洋受平均翻轉環流 (time-mean overturning circulation) 控制與東太平洋受反氣旋式羅士培波碎裂 (anticyclonic Rossby wave breaking) 影響。準確來說，在西、中太平洋較強的噴流抑制了該區的羅士培波碎裂，這使此處有較強風切渦度的帶狀副熱帶高壓被熱帶對流透過熱力驅動區域哈德里胞 (thermally-driven local Hadley cell) 以及噴流出區的地轉調整環流所主導。另一方面，相較於西邊的強西風噴流，東太平洋較弱的西風以及其伴隨的位渦 (potential vorticity) 梯度使此處容易發生羅士培波碎裂。透過羅士培波碎裂的合成分析，我們也發現波動碎裂可以加強東太平洋局部的沉降進而使該區有更強的曲率渦度與封閉反氣旋環流。針對副熱帶高壓的季節轉換，我們發現東太平洋有較強曲率渦度的封閉高壓在冬季轉春季時於中太平洋明顯的快速向西擴張，而此西擴可歸因於中太平洋的噴流於此時期減小，並與南半球熱帶加熱的削弱有關。此季節轉換的分析也進一步支持我們將噴流視為副熱帶高壓控制因子的猜想。而這樣由噴流參與其中的概念不只揭示了冬季北太平洋副熱帶高壓的控制因子，也為研究外熱帶-熱帶交互作用的過程提供了可能的框架。

關鍵字：

北太平洋副熱帶高壓、羅士培波碎裂、哈德里胞、東亞西風噴流



## Abstract



This study investigates the controlling factors of the North Pacific subtropical high, focusing on boreal winter and the rapid transition in spring. We show that the jet in the Pacific basin plays a critical role in controlling the strength and the location of the North Pacific subtropical high. Specifically, the zonal differences in the jet strength lead to two distinct sources of subsidence in winter: the time-mean overturning in the west and the anticyclonic Rossby wave breaking in the east. The strong jet in the western and central North Pacific inhibits wave breaking. The subtropical high belt with strong shear vorticity in this region is then controlled by the tropical convection through the thermally-driven local Hadley cell and the time-mean geostrophic adjustment at the jet exit region. On the other hand, the weak jet and associated PV gradient in the eastern Pacific result in higher wave breaking frequency. The composite analysis of Rossby wave breaking days further suggests the strengthening effect of wave breaking on the local subsidence and the closed anticyclone with relatively strong curvature vorticity. From winter to spring, the closed anticyclone in the eastern Pacific rapidly expands westward, which can be attributed to the weakening of the jet and the upstream Southern Hemispheric tropical heating. The seasonal transition supports the hypothesis of the jet in controlling the North Pacific subtropical high in winter. The proposed concept of the jet-mediated controlling factor of

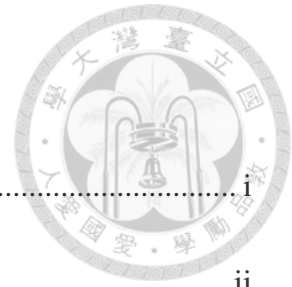
the subtropical high also provides a framework to investigate the mechanisms of the extratropical-tropical interaction.



Keywords:

North Pacific subtropical high, Rossby wave breaking, Hadley cell, East Asian jet

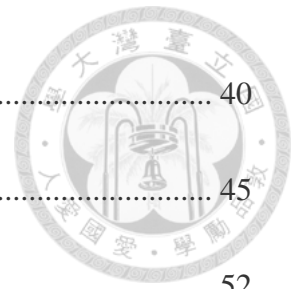
# Contents

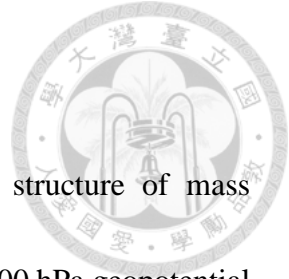


致謝 .....	i
中文摘要 .....	ii
Abstract.....	iv
Contents .....	vi
List of Figures.....	viii
1. Introduction .....	1
2. Data and Methods .....	7
2.1 Data Description .....	7
2.2 Dynamical Constraint on the Thermally-Driven Divergent Circulation .....	8
2.3 Theoretical Boundary of Thermally-driven Hadley Cell .....	10
2.4 Seasonal Mean Ageostrophic Wind Budget Decomposition .....	12
2.5 Wave Activity Flux .....	15
2.6 Identification of Anticyclonic Rossby Wave Breaking.....	15
3. The Wintertime Circulation.....	18
3.1 The Role of the Thermally-driven Local Hadley Cell on Basin Scale .....	18
3.2 The Influence of Rossby Wave Breaking on the Anticyclone .....	24
3.3 The Unified Controlling Factor: Westerly Jet in the Pacific Basin.....	29
4. The Transition from Winter to Spring.....	33



5. Conclusion and Discussion.....	40
References .....	45
Figures .....	52





## List of Figures

**Fig. 1.1** Climatology of **(top)** the globally zonal mean vertical structure of mass streamfunction (contour) and  $\omega$  (shading) and **(bottom)** 900 hPa geopotential height (contour; unit: m), lower-tropospheric  $\omega$  (shading), and high ridge (thick black line). The left, central, and right columns are January, April, and July, respectively. The contour interval in the top row is  $4 \times 10^{10}$  kg/s. The lower-tropospheric  $\omega$  in the bottom row is mass-weighted vertical averaged  $\omega$  from 700 to 900 hPa.

**Fig. 2.1** Illustration of the Rossby wave breaking identification algorithm. 2PVU isolines (green and black lines) and regions of stratospheric PV folding (color) on 28<sup>th</sup> Jan. 2000. The longest 2PVU isoline on each isentrope over the globe is marked as the green line. The blue (red) colored patches are regions of anticyclonic (cyclonic) Rossby wave breaking regions.

**Fig. 3.1** DJF climatology of 200 hPa local  $Ro$  (shading; unit: 1), 900 hPa geopotential height (green contour), and subtropical high ridge (green dashed line). The local  $Ro = 0.5$  isolines are shown as thick black lines to indicate the region of the thermally-driven regime. The contour interval of the geopotential high is 20m with thickened 1050m isolines.

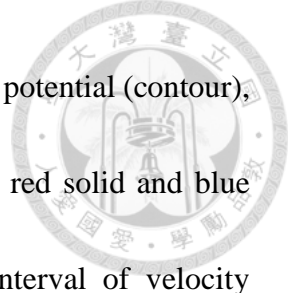
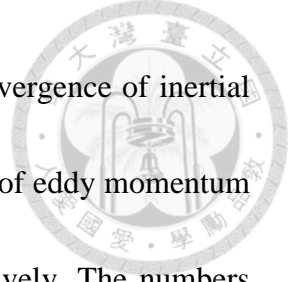


**Fig. 3.2** DJF climatology of 200 hPa divergence (shading), velocity potential (contour), divergent wind (arrow), and subtropical high ridge (thick red solid and blue dashed line) in the North Pacific basin. The contour interval of velocity potential is  $2 \times 10^6$  m<sup>2</sup>/s. The unit of divergent wind is m/s. The red solid and blue dashed lines are the actual and theoretical ridge lines of zero surface zonal wind, respectively.

**Fig. 3.3** DJF climatology of 200 hPa meridional wind (shading) and zonal wind (contour; unit: m/s). The meridional winds in the upper row denote (a) actual divergent wind,  $\bar{v}_d$ , and (b) actual ageostrophic wind,  $\bar{v}_{a,act}$ . (c)-(e) are estimated ageostrophic wind,  $\bar{v}_{a,est}$ , by (c) zonal wind inertial advection,  $\bar{u} \cdot \partial\bar{u}/\partial\lambda \cdot (fa \cos \phi)^{-1}$ , (d) meridional wind inertial advection,  $\bar{v} \cdot \partial\bar{u}/\partial\phi \cdot (fa)^{-1}$ , and (e) transient eddy momentum flux divergence. (f) is the difference between  $\bar{v}_{a,act}$  and  $\bar{v}_{a,est}$ . The  $\bar{v}_{a,est}$  is the summation of (c)-(e). Due to the validity of quasi-geostrophic approximation, the region equatorward of 15°N is ignored and masked for the terms related to  $\bar{v}_a$ .

**Fig. 3.4** DJF climatology of 200 hPa divergence contributed by different terms in ageostrophic wind decomposition over the subtropical central Pacific ([150°E~150°W, 15°N~30°N]). The divergence considers both meridional and zonal directions. The three terms in the middle denote the zonal divergence



of inertial advective  $\bar{u}_a$  ( $-(\bar{\mathbf{v}} \cdot \nabla)\bar{v}/f$ ), the meridional divergence of inertial advective  $\bar{v}_a$  ( $(\bar{\mathbf{v}} \cdot \nabla)\bar{u}/f$ ), and the horizontal divergence of eddy momentum flux divergence ( $\langle -\nabla \cdot (\overline{\mathbf{v}'v'})/f, \nabla \cdot (\overline{\mathbf{v}'u'})/f \rangle$ ), respectively. The numbers below the bars are the percentages of contribution from different terms to the total divergence of ageostrophic wind.

**Fig. 3.5** (upper) DJF climatology of 900 hPa (a) curvature and (b) shear vorticity (shading) and geopotential height (contour; unit: m). (bottom) The annual cycle of the  $\pm 5$ -day running mean zonal mean 900 hPa (c) curvature and (d) shear vorticity in the central Pacific sector ( $160^\circ\text{E} \sim 160^\circ\text{W}$ ).

**Fig. 3.6** DJF climatology of the jet and Rossby wave waveguide. (a) 300 hPa zonal wind (shading) and 2PVU isolines on 310K to 350K isentropes (blue lines). (b) Anticyclonic Rossby wave breaking frequency summed over 310K to 350K (shading), 300 hPa zonal wind (contour), and stationary WAF (arrow).

**Fig. 3.7** Weather map on 7<sup>th</sup> Jan. 2000. (a) 250 hPa anomalous meridional wind relative to DJF climatology (shading) and 340K PV (contour; 2, 3, and 4 PVU). (b) precipitation (shading), lower-tropospheric  $\omega$  ( $\omega_{lt}$ , grey crosses), 900 hPa geopotential height (contour), and 2PVU isolines on 320K – 340K isentropes (thick red lines). The  $\omega_{lt}$  is mass-weighted vertical averaged  $\omega$  from 500 to 700 hPa and only shown over the regions of  $\omega_{lt} \geq 0.04$  Pa/s. The contours of

geopotential height start from 1030m with an interval of 40m and thickened 1090m contour. The 2PVU isolines on 320K – 340K isentropes with 10K intervals are in crimson, orange, red, and dark red, respectively.



**Fig. 3.8** Anticyclonic Rossby wave breaking features on (**upper**) 340K and (**lower**) 320K isentropes over the North Pacific basin ( $120^{\circ}\text{E}\sim 100^{\circ}\text{W}$ ). (**left**) The Rossby wave breaking object-centered composite of anomalous 900 hPa geopotential height (shading), anomalous precipitation (blue contour), anomalous  $\omega_{lt}$  (orange contour), and actual PV (black contour; unit: PVU). Only the precipitation ( $\omega_{lt}$ ) anomalies larger than 1 mm/day (0.04 Pa/s) are shown with contour interval of 1.5 mm/day (0.04 Pa/s). The statistically significant ( $p=5\%$ ) anomalous geopotential height, precipitation, and  $\omega_{lt}$  are denoted by grey dots, thick blue, and thick orange contours, respectively. (**right**) two-dimensional histogram of the occurrence of anticyclonic Rossby wave breaking centroid within each  $5^{\circ} \times 5^{\circ}$  box over the North Pacific basin. The summation of the values in colored regions is 100% of the anticyclonic Rossby wave breaking days on each isentrope.

**Fig. 3.9** The composite of 900 hPa geopotential height on (a) 340K, (b) 320K anticyclonic Rossby wave breaking days, and (c) non-Rossby wave breaking days. The shading in (c) are the actual values while in (a) and (b) are anomalies

relative to climatology (contour) with grey dots for statistical significance (p=5%).



**Fig. 3.10** The composite of zonal mean anomalous zonal wind (shading), anomalous vertical circulation ( $\langle v, \omega \rangle$ , arrow), and actual isentropes (contour) on (a) 340K and (b) 320K anticyclonic Rossby wave breaking days in the chosen sectors. The sector for the certain isentrope is a  $30^\circ$  wide band centered at the longitude of the maximum anticyclonic Rossby wave breaking frequency on the given isentrope. The grey dots denote the statistically significant (p=5%) anomalous zonal wind.

**Fig. 3.11** As in **Fig. 3.4**, but for divergence over the subtropical eastern Pacific.

**Fig. 3.12** DJF climatology of zonal wind (shading), isentropes (black contour; unit: K), 2PVU isoline (thick grey line), and meridional overturning circulation ( $\langle \bar{v}_d, \bar{\omega} \rangle$ , arrow) zonally averaged in (a)  $160^\circ\text{E}\sim 180^\circ$  and (b)  $140^\circ\text{W}\sim 120^\circ\text{W}$ .

**Fig. 4.1** Seasonal evolution of the circulation features in the North Pacific basin. (a)  $\pm 5$ -days running mean of curvature vorticity averaged over anticyclonic regions in the central Pacific (blue) and its  $\pm 15$ -days running tendency (pink). (b), same as (a) but for shear vorticity. (c) 200 hPa local Ro averaged over the subtropical region in different longitudinal sectors.

**Fig. 4.2** As in **Fig. 1.1d**, but for differences between April and January.



**Fig. 4.3** Climatology of 200 hPa divergence (shading), zonal wind (contour), and divergent wind (arrow) in (a) January, (b) April, and (c) their differences between April and January.

**Fig. 4.4** As in **Fig. 3.4**, but for the region over subtropical eastern central Pacific. The blue, green, and pink bars represent January, April, and the differences between April and January, respectively. The percentages below the bar are for the differences between months.

**Fig. 4.5** Hovmöller diagram of the column-integrated apparent heat source ( $Q_1$ ) meridionally averaged over  $20^{\circ}\text{S}\sim 0^{\circ}$ . The column-integrated values are mass-weighted vertical averaged  $Q_1$  from 70 hPa to surface. A  $\pm 5$ -days running mean is applied to the column-integrated  $Q_1$  field.

**Fig. 4.6 (upper)** Climatology of anticyclonic Rossby wave breaking frequency (shading), zonal wind (black contour) on 340K isentrope and 900 hPa geopotential height (green contour) in (a) January, (b) April, and (c) their differences between April and January. The isentropic zonal wind is contoured in (a) and (b) in levels of 10, 20, 30, 40, 50, 70 m/s and in (c) with interval of 10 m/s. The contour intervals of 900 hPa geopotential height are 20 m in (a) and (b) and 40 m in (c). **(lower)** Climatology of meridionally averaged anticyclonic Rossby wave breaking frequency on each isentrope. The average

is taken over  $0^{\circ}\sim 60^{\circ}\text{N}$ . The thin vertical lines are the longitude of maximum wave breaking frequency.



**Fig. 4.7 (upper)** The composite of 900 hPa geopotential height anomalies on 340K anticyclonic Rossby wave breaking days (shading) and the climatology of geopotential height (contour) in (a) January, (b) April, and (c) their differences between April and January. The contour intervals of 900 hPa geopotential height are 20 m in (a) and (b) and 40 m in (c). The statistically significant ( $p=5\%$ ) anomalies are denoted by grey dots. **(lower)** As in the upper row, but for the composite of 320K anticyclonic Rossby wave breaking days.

**Fig. 5.1** Summary schematics of the jet-mediated controlling factor of the North Pacific subtropical high in winter and spring. The figures on the left and right are the vertical profile of zonal wind (shading), isentropes (contour), and 2PVU isolines (grey line) in the central and eastern Pacific.

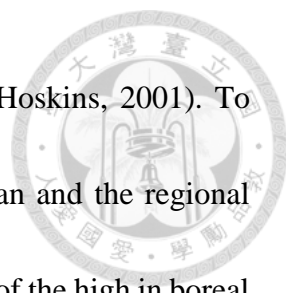




## 1. Introduction

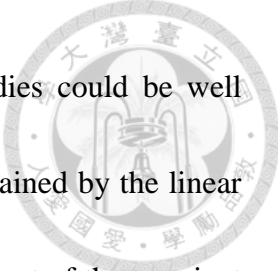
The subtropical highs are lower-tropospheric anticyclonic circulations occupying the subtropical oceans. These circulations play an important role in the planetary scale's moisture transport (Li et al., 2011) and radiative balance (Klein et al., 1995). Moreover, recent studies have shown that under global warming, the change of the subtropical high would impact the regional climate and local society (Cherchi et al., 2018; Song et al., 2018). Therefore, clarifying the controlling factors of the subtropical high is a top issue for understanding the earth system in the present or even in the future under anthropogenic climate change.

Conventional wisdom regards the subtropical high as a result of the subsidence branch from the global Hadley cell. However, this view of globally zonal mean circulation is insufficient for understanding the circulation in a single basin. As described in the inquiry raised by E. Sarachik and demonstrated in Figure 1.1, the Hadley cell in the Northern Hemisphere reaches its maximum strength in boreal winter and becomes weaker from winter to summer (solid contour showing meridional mass streamfunction and orange shading plotting subsidence in Fig. 1.1a, 1.1b, and 1.1c). On the contrary, the North Pacific subtropical high in winter is the weakest throughout the seasonal cycle and is only confined in the eastern Pacific (contour in Fig. 1.1d). When the season evolves into boreal summer, the North Pacific subtropical high becomes stronger (Fig. 1.1e and



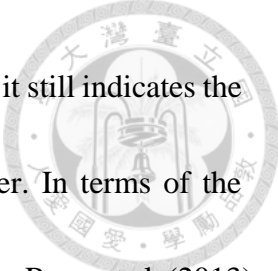
1.1f) and occupies nearly 40% of the earth's surface (Rodwell & Hoskins, 2001). To explain this inconsistency in the seasonality between the zonal mean and the regional perspectives, previous studies investigated the formation mechanism of the high in boreal summer and emphasized the role of time-averaged zonal asymmetric heating in subtropical regions (Chen et al., 2001; Liu et al., 2004; Rodwell & Hoskins, 2001; Seager et al., 2003; Ting, 1994). Rodwell & Hoskins (2001) show that the strong diabatic heating on the continent in summer leads to the subsidence to the west of the heating and hence the equatorward lower-tropospheric wind through Sverdrup balance. Via the potential vorticity (PV) perspective, Liu et al. (2004) further demonstrate that the quadruple diabatic heating pattern in the subtropics provides the vorticity source of the lower-tropospheric circulation in summer. This group of literature has stated the importance of the subtropical zonal asymmetric heating to the North Pacific subtropical high in boreal summer, the mechanism of the wintertime circulation and the rapid seasonal transition in spring remain to be explored.

For the North Pacific subtropical high in winter, previous studies have interpreted it as a result of stationary Rossby waves forced by orography and diabatic heating (Chen, 2005; Held et al., 2002; Rodwell & Hoskins, 2001). Held et al. (2002) summarize the usefulness of this viewpoint by presenting the stationary eddy streamfunction from both linear and nonlinear stationary wave models relative to the zonally uniform background




flow. Their results suggest that the actual low-level stationary eddies could be well captured by the response to diabatic heating and orography and explained by the linear theory of stationary Rossby waves. They further state the limited impact of the transient eddy vorticity fluxes on their low-level stationary wave structure. Rodwell & Hoskins (2001) also highlight the role of the nonlinear response of the strong background westerlies to the Rocky Mountains in the eastern-confined North Pacific subtropical anticyclone in winter.

Being different from the view of the temporal-mean forcing, recent studies have pointed out the possible role of midlatitude transient eddies in influencing the subtropical high (Aemisegger et al., 2021; Nigam & Chan, 2009; Ryoo et al., 2013). Nigam & Chan (2009) show that the change in midlatitude storm track is important to the winter-to-summer transition of the North Pacific subtropical high. Their linear primitive equation model suggests that the abatement of the wintertime eddy heat and momentum flux over the storm track region is the main contributor to the increasing high in the extratropics during the transition seasons. This implies the importance of midlatitude transient eddies to the eastern-confined subtropical anticyclone in winter. Additionally, Aemisegger et al. (2021) utilize the observational data and the backward trajectories to demonstrate that more than half of the mass source in the subtropical North Atlantic in winter comes from the extratropics through Rossby wave breaking-induced isentropic downgliding.



Although their results focus on the feature in the North Atlantic basin, it still indicates the relevance of Rossby wave breaking to the subtropical high in winter. In terms of the interannual variability of the circulation in the subtropical North Pacific, Ryoo et al. (2013) show that El Niño-Southern Oscillation could influence the preferred Rossby wave breaking type and hence the subtropical high in the eastern Pacific. These findings all suggest a potential role of midlatitude transient Rossby waves on the wintertime North Pacific subtropical high. In summary, previous studies have regarded the North Pacific subtropical high in winter as the result of forced stationary Rossby wave and transient Rossby wave breaking. However, the contribution from the aforementioned strongest global Hadley cell in winter has been barely identified in previous literature. Moreover, how and where the Rossby wave breaking influences the climatology of the wintertime North Pacific subtropical high remain to be explored. These gaps between different agents indicate a more comprehensive examination of the controlling factor of the subtropical high in boreal winter is required. This more thorough understanding of the controlling factor in winter could also help explain the seasonal cycle of the high itself.

For the seasonal transition of the North Pacific subtropical high, previous studies have focused on the evolution from winter to summer. This transition is interpreted as the consequence of the increasing summertime zonal asymmetric heating (Rodwell & Hoskins, 2001; Seager et al., 2003) and the weakening wintertime storm track (Nigam &



Chan, 2009). Yet, as shown in the upper panel of Figure 4 in Nigam & Chan (2009), the high in the subtropical central Pacific shows a peak strength in April rather than July as the feature in the midlatitudes discussed in previous literature. Furthermore, their Figure 2 shows that the evolution of the subtropical closed anticyclone seems to be two-stage: expanding westward from January to May and northward from May to July. This evolution indicates that the seasonal transition of the North Pacific subtropical high is not fully understood, especially for the high in the subtropical central Pacific from winter to spring.

The objective of this study is twofold. First, we investigate factors controlling the wintertime North Pacific subtropical high, establishing a unified view by considering the effect of both the thermally-driven time-mean overturning circulation and the Rossby wave breaking together. Secondly, we seek to provide a mechanistic understanding of its winter-to-spring transition that is relatively less addressed. The winter-to-spring transition of the high could serve as an examination of the controlling factor we identified in boreal winter. To reach these goals, we analyze the 18-year climatology of the reanalysis data from the European Center for Medium-Range Weather Forecasts (ECMWF). Details of the reanalysis dataset and other methods we applied are described in Chapter 2. In Chapter 3, we demonstrate the controlling factors of the North Pacific subtropical high in boreal winter, including the contribution from the thermally-driven local Hadley cell (Chapter

3.1), the influence of Rossby wave breaking (Chapter 3.2), and the unified controlling factor (Chapter 3.3). The seasonal transition of the North Pacific subtropical high from winter to spring and its relationship with the change in the controlling factors we identified in winter is demonstrated in Chapter 4. Finally, the physical interpretation of our results and its implication for the general circulation theory are discussed and summarized in Chapter 5.



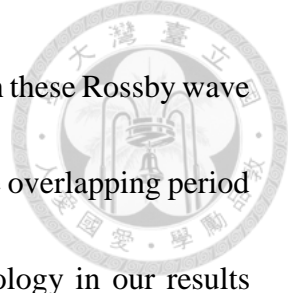


## 2. Data and Methods

In this chapter, we describe the reanalysis and observational data utilized for investigating the formation of climatology (Chapter 2.1) and introduce the methods applied to the data and the background information for the physical meaning of each method (Chapters 2.2 ~ 2.6). Chapters 2.2 and 2.3 explain how we identify the location of theoretical thermally-driven local Hadley cell in the North Pacific basin via the upper-tropospheric dynamical constraint and the convective quasi-equilibrium theory. To separate the contribution from time-mean flow and eddies, the decomposition of the ageostrophic wind budget is presented in Chapter 2.4. Chapters 2.5 and 2.6 then introduce the methods for detailed information about the Rossby waves and wave breaking.

### 2.1 Data Description

In this study, we use monthly and daily mean isobaric data from the Interim ECMWF Re-Analysis dataset (ERA-Interim; Dee et al., 2011) for our analysis of the climatology. Daily mean isentropic data from ERA-Interim is also used to identify the Rossby wave breaking events. The ERA-Interim data are all performed at  $0.75^\circ \times 0.75^\circ$  resolution. Compared to previous studies identifying Rossby wave breaking (Homeyer & Bowman, 2013; Wernli & Sprenger, 2007), this horizontal resolution is sufficient for detecting wave breaking objects. The daily mean precipitation data from version 1.3 of the Global Precipitation Climatology Project (GPCP; Huffman et al., 2001) with the resolution of



$1^\circ \times 1^\circ$  is also used to represent the ascending motion associated with these Rossby wave breaking events. To have the same reference for climatology, only the overlapping period of these two datasets are included in our study. Hence, the climatology in our results considers only the period from 1997 to 2014 (18 years).

## 2.2 Dynamical Constraint on the Thermally-Driven Divergent Circulation

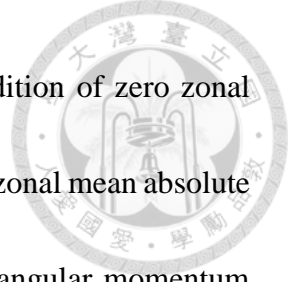
We seek to recognize the regions directly controlled by the strong Northern Hemispheric Hadley cell in boreal winter. Schneider & Bordoni (2008) have suggested that the Hadley cell in the winter hemisphere is mainly thermally-driven. The regions dominated by the thermally-driven Hadley cell could be identified by the dynamical constraint of the upper-tropospheric momentum and vorticity budget that is well-described in the conventional theory of the globally zonal mean Hadley cell (Held & Hou, 1980; Lindzen & Hou, 1988; Schneider, 2006).

Under a zonal mean framework, the temporal mean zonal mean circulation strength could be described by the zonal momentum budget in the upper branch of the circulation, in which the vertical advection is negligible, (eq.1 in Walker & Schneider, 2006)

$$(f + [\bar{\zeta}])[\bar{v}] = \mathcal{S} \quad (2.1)$$

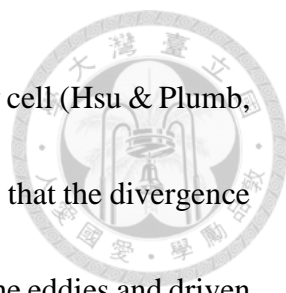
where  $f$  is planetary vorticity,  $\zeta$  is relative vorticity,  $v$  is meridional wind,  $\mathcal{S}$  is the eddy momentum flux divergence,  $\bar{(\cdot)}$  is temporal mean, and  $[\cdot]$  is zonal mean. For the circulation in the nearly inviscid limit with no effect of transient eddies, the circulation is purely driven by thermal forcing and the right-hand side (RHS) of (2.1) equals zero. This





indicates that the thermally-driven circulation exists under the condition of zero zonal mean absolute vorticity (Emanuel, 1995; Schneider, 2006). Since the zonal mean absolute vorticity is proportional to the meridional gradient of the absolute angular momentum about the earth's axis,  $-(a^2 \cos \phi)^{-1} \partial_{\phi} M = f - (a \cos \phi)^{-1} \partial_{\phi}([\bar{u}] \cos \phi) = f + [\bar{\zeta}] = [\bar{\eta}]$ , with absolute angular momentum  $M = (\Omega a \cos \phi + u) a \cos \phi$ , angular velocity of planetary rotation  $\Omega$ , earth radius  $a$ , latitude  $\phi$ , and zonal wind  $u$ , the temporal mean circulation conserves its absolute angular momentum. This conservation is identical to the thermally-driven Hadley cell described in Held & Hou (1980). For the circulation considering the effect of the eddies, the eddy momentum flux divergence is involved in the zonal momentum balance and the absolute vorticity deviates from zero. The degree of the influence from eddies to the mean overturning could be measured by local  $Ro$ , a non-dimensional parameter defined as  $-[\bar{\zeta}]/f$ , describing the relative importance of nonlinear advection of mean flow and Coriolis force to the zonal momentum budget. When local  $Ro$  reaches zero, the nonlinear effect from mean flow advection is negligible and the circulation is purely driven by eddies. On the contrary, the local  $Ro \sim 1$  indicates the regions of the thermally-driven circulation.

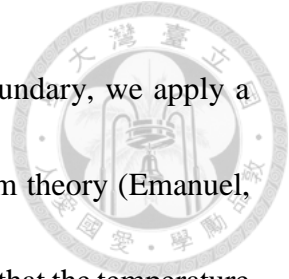
Extending the concept of the dynamical constraint on the thermally-driven overturning from the zonal mean framework into three-dimensional circulation, previous studies have shown that the thermally-driven divergence is enclosed by the zero absolute



vorticity contour as the feature seen in the globally zonal mean Hadley cell (Hsu & Plumb, 2000; Schneider, 1987; Zhai & Boos, 2015). This constraint indicates that the divergence within a patch of zero absolute vorticity (local  $Ro \sim 1$ ) is unrelated to the eddies and driven by thermal forcing. We then utilize the spatial distribution of local  $Ro$  as an indicator for thermally-driven overturning circulation. That is, in the regions of  $Ro \sim 1$ , the circulation is unstable and effectively driven by thermal forcing. However, we note that deviation from  $Ro \sim 1$  is only the necessary but not the sufficient condition for the eddy-driven circulation. This means that the upper-tropospheric vorticity could be balanced by thermally forced stationary Rossby wave in regions of  $Ro \approx 1$  but not transient eddies. Deviation from  $Ro \sim 1$  only implies a potential of the eddy-driven overturning circulation in the three-dimensional framework. Nevertheless, local  $Ro$  is still a useful parameter for identifying the three-dimensional thermally-driven circulation. For any regions with local  $Ro \sim 1$ , the divergence is purely driven by thermal forcing and the circulation is under a thermally-driven regime. For any circulation affected by eddy forcing, the local  $Ro$  deviates from one.

### **2.3 Theoretical Boundary of Thermally-driven Hadley Cell**

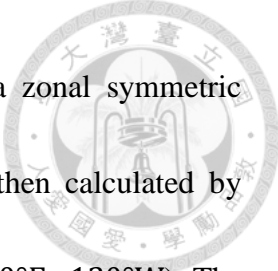
In Chapter 2.2, we introduce the method for recognizing regions of upper tropospheric thermally-driven divergence, we then focus on the lower level theoretical boundary of the thermally-driven Hadley cell to identify the location of the direct



influence from the tropical circulation. To obtain the theoretical boundary, we apply a calculation following the concept of the convective quasi-equilibrium theory (Emanuel, 1995) to our reanalysis data in the Pacific sector. This theory assumes that the temperature structure of the tropical free atmosphere is controlled by boundary layer entropy,  $s_b$ . The vorticity at the tropopause level is then determined by the profile of  $s_b$  through thermal wind balance. According to Emanuel (1995), when  $f\eta < 0$  at the tropopause, the atmosphere is unstable and requires thermally direct circulation to adjust the entropy distribution. Hence, there is a critical profile of  $s_b$  that the atmosphere reaches single column radiative-convective equilibrium and  $f\eta = 0$  at the tropopause (eq.11 in Emanuel, 1995). The thermally direct circulation then depends on the supercriticality of the actual  $s_b$  profile. The zonal mean surface zonal wind of the thermally-driven meridional circulation could be described as eq.18 in Emanuel (1995), which is

$$u_s = \frac{T_s - T_t}{2\Omega a \sin \phi} \frac{\partial}{\partial \phi} (s_b - s_{b,crit}) \quad (2.2)$$

, where  $T_s$  and  $T_t$  are the temperatures at the surface and the tropopause, respectively;  $s_{b,crit}$  is the  $s_b$  critical meridional profile of single column radiative-convective equilibrium. The more the actual  $s_b$  profile deviates from the critical profile, the stronger the theoretical thermally-driven circulation adjustment exists. The poleward boundary of the thermally-driven Hadley cell could then be identified as the latitude of zero surface zonal wind.



Since (2.2) only describes the meridional circulation under a zonal symmetric condition, the regional Hadley cell in the North Pacific basin is then calculated by applying (2.2) onto the zonal mean  $s_b$  within the Pacific sector ( $120^\circ\text{E}\sim 120^\circ\text{W}$ ). The  $s_b$  in our analysis is written as  $c_p \ln \theta_{eb}$  (as the form in Emanuel, 1995), where  $c_p$  is the heat capacity at constant pressure and  $\theta_{eb}$  is the equivalent potential temperature at the lowest pressure level, which is about 1000 ~ 950 hPa depending on the actual surface pressure. This terrain-following approach is analogous to the strategy used in Nie et al. (2010). We have examined the sensitivity of the  $s_b$  meridional structure to the selected pressure levels. Our results show that it is insensitive to the chosen level if the pressure level is under 925 hPa, which is a common level in previous studies discussing the effect of subcloud layer entropy under convective quasi-equilibrium theory (Shaw & Voigt, 2016a, 2016b).

#### **2.4 Seasonal Mean Ageostrophic Wind Budget Decomposition**

In the previous two chapters, we only focus on identifying the presence of the thermally-driven time-mean flow. Here, we seek to quantify the contribution from not only the time-mean flow but also the eddies to the seasonal mean upper-tropospheric convergence and the overturning circulation. For this purpose, a seasonal mean ageostrophic wind budget decomposition is applied to the upper-tropospheric reanalysis data. According to quasi-geostrophic approximation, in the midlatitudes and subtropical



regions, the upper-tropospheric convergence is mainly contributed by the convergence of ageostrophic wind. The balance of the time-mean ageostrophic wind could be approximated by the horizontal momentum equation of a Bousseniq, adiabatic fluid as the first two equations of eq.A10 in Hoskins et al. (1983)

$$\begin{cases} \frac{D\bar{u}}{Dt} = f\bar{v} - \bar{\Phi}_x - \nabla \cdot (\bar{\mathbf{v}'u'}) \\ \frac{D\bar{v}}{Dt} = -f\bar{u} - \bar{\Phi}_y - \nabla \cdot (\bar{\mathbf{v}'v'}) \end{cases} \quad (2.3)$$

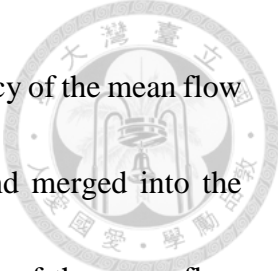
where  $\mathbf{v} = \langle u, v \rangle$  is the horizontal velocity,  $\Phi$  is the geopotential, and  $\bar{(\cdot)}$  and  $(\cdot)'$  is the seasonal mean and daily deviation from this mean, respectively. The subscript denotes the direction of the horizontal gradient. With the definition of the total derivative and ageostrophic wind,  $\bar{\mathbf{v}}_a = \bar{\mathbf{v}} - f^{-1}\hat{\mathbf{k}} \times \nabla \bar{\Phi}$ , (2.3) can be rewritten as

$$\begin{cases} \frac{\partial \bar{u}}{\partial t} = f\bar{v}_a - (\bar{\mathbf{v}} \cdot \nabla)\bar{u} - \nabla \cdot (\bar{\mathbf{v}'u'}) \\ \frac{\partial \bar{v}}{\partial t} = -f\bar{u}_a - (\bar{\mathbf{v}} \cdot \nabla)\bar{v} - \nabla \cdot (\bar{\mathbf{v}'v'}) \end{cases}$$

The ageostrophic wind can then be decomposed into

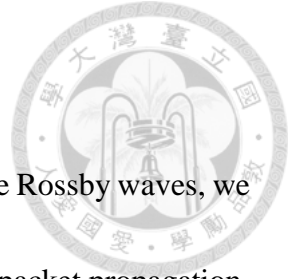
$$\begin{cases} \bar{v}_a = \left( (\bar{\mathbf{v}} \cdot \nabla)\bar{u} + \nabla \cdot (\bar{\mathbf{v}'u'}) + \frac{\partial \bar{u}}{\partial t} \right) f^{-1} \\ \bar{u}_a = \left( -(\bar{\mathbf{v}} \cdot \nabla)\bar{v} - \nabla \cdot (\bar{\mathbf{v}'v'}) - \frac{\partial \bar{v}}{\partial t} \right) f^{-1} \end{cases} \quad (2.4)$$

The three terms on the RHS are the inertial advection from the mean flow, the horizontal divergence of eddy momentum flux, and the mean flow tendency, respectively. The upper-tropospheric ageostrophic divergence is then calculated by the horizontal divergence of each term in (2.4) on the spherical coordinate.



Since we consider only the seasonal mean circulation, the tendency of the mean flow is negligible (smaller than 1 order of magnitude of other terms) and merged into the residual of the decomposition in our analysis. The physical meaning of the mean flow inertial advection is similar to the geostrophic adjustment at the jet exit region in the jet streak analysis. Therefore, the decomposition of the ageostrophic wind could be interpreted as the time-mean inertial advection by the jet and the explicitly eddy-driven components. Although the contribution from high- and low-frequency eddies to the mean momentum budget are distinct from each other (Chan et al., 2020), here we consider the effect of eddies as a whole. Thus, the eddy term is not decomposed into contributions from different frequencies in our budget analysis.

We note that the concept of this budget decomposition is related but not equal to the dynamical constraint introduced in Chapter 2.2. The decomposition here aims to distinguish the contribution from transient eddies and the time-mean flow, but not to identify the direct thermally-driven divergence. Instead, the direct thermally-driven divergence in the patch of zero absolute vorticity is combined with the effect of stationary Rossby wave into the mean flow advection terms in our current budget. Decomposing these two thermal effects is, however, out of the scope of our current budget analysis.



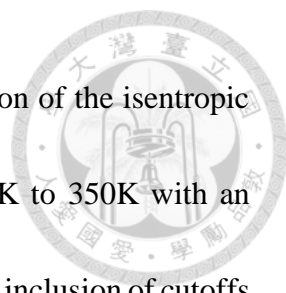
## 2.5 Wave Activity Flux

For more detailed information about the eddies, especially for the Rossby waves, we calculate the wave activity flux (WAF) to illustrate the Rossby wave packet propagation.

In this study, we follow eq.38 in Takaya & Nakamura (2001) and assume that the phase-propagating speed along with the mean flow,  $C_U$ , is zero for the stationary WAF we are interested in. The stationary WAF in the following analysis is then calculated by the daily mean anomalous streamfunction after applying an 8-day low-pass Lanczos filter. The anomalies are derived as the deviation from the zonally varying reference field which is defined as the climatology from 1997 to 2014. To represent the horizontal propagation of the Rossby waves at the tropopause level and avoid the sharp vertical PV gradient above and near the tropopause, only the horizontal WAF on 300 hPa is considered in the following analysis.

## 2.6 Identification of Anticyclonic Rossby Wave Breaking

Previous studies have shown that the PV streamer or PV folding is a common signature to be seen at the end of the life cycle of breaking Rossby waves (Homeyer & Bowman, 2013; Postel & Hitchman, 1999; Wernli & Sprenger, 2007). Here, we follow the concept of the algorithm identifying Rossby wave breaking in Homeyer & Bowman (2013). The Rossby wave breaking is identified by the folding of the isentropic PV isoline each day. The PV value of the isoline is chosen to be 2PVU since this is the conventional



usage of the dynamic tropopause. Due to the coarse vertical resolution of the isentropic data, the data is linearly interpolated onto the isentropes from 310K to 350K with an interval of 10K before the searching of the 2PVU isoline. To avoid the inclusion of cutoffs, we only consider the folding along the longest 2PVU isoline over the globe on each isentrope (green lines in Fig. 2.1). The PV folding objects are then identified as regions with meridians intersecting the 2PVU isoline more than two times and enclosed by the PV isoline. To avoid noises from fragmented folding objects, the identified objects whose boundaries are closer than  $3^\circ$  longitudes are combined first, and the combined objects spanning less than  $5^\circ$  longitudes are then recognized as noises and excluded. The PV folding objects, or Rossby wave breaking objects, are identified as the shaded patches in Figure 2.1. Previous studies have shown that anticyclonic Rossby wave breaking prefers to occur on the subtropical flank of the jet (Martius et al., 2007; Ryoo et al., 2013; Thorncroft et al., 1993). Hence, to discuss the impact of Rossby wave breaking on the subtropical high, we only focus on the anticyclonic wave breaking (blue shaded area in Fig. 2.1) in the following analysis.

To validate our algorithm for detecting Rossby wave breaking, we also compare our results to the monthly features of the climatological PV streamer dataset provided by ETH Zürich (Sprenger et al., 2017). Although the magnitude of the wave breaking frequencies from our algorithm are smaller than those in the ETH Zürich dataset which might be due



to the stricter criterion for PV folding than PV streamer, the pattern is qualitatively similar in both datasets. This agreement suggests that our algorithm is comparable with previous studies and sufficient for our investigation.






### **3. The Wintertime Circulation**

As shown in Figure 1.1d and described by the Sarachik inquiry, the relatively weak North Pacific subtropical closed anticyclone in boreal winter is confined in a relatively small area in the eastern Pacific and seemingly inconsistent with the strong Northern Hemispheric Hadley cell in winter. To provide a comprehensive mechanism of the wintertime subtropical high, we first identify the contribution from the strong Hadley cell to the high in Chapter 3.1. The controlling factors of the closed anticyclone in the eastern Pacific with the focus on the role of Rossby waves are then clarified in Chapter 3.2. A unified factor that considers both the effects discussed in Chapters 3.1 and 3.2 are performed in Chapter 3.3.

#### **3.1 The Role of the Thermally-driven Local Hadley Cell on Basin Scale**

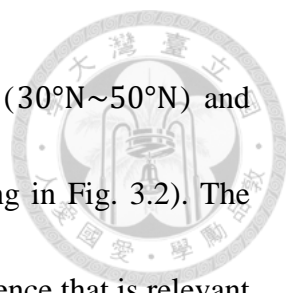
Under the zonal mean framework, the Hadley cell in winter is mainly driven by thermal forcing (Schneider & Bordoni, 2008). As introduced in Chapter 2.2, the regions of the three-dimensional thermally-driven Hadley cell are at where the local  $Ro \sim 1$ . Hence, we calculate the climatological DJF 200 hPa local  $Ro$  over the North Pacific to identify the regions controlled by the thermally-driven Hadley cell. Figure 3.1 shows that the local  $Ro$  over the subtropical western North Pacific ( $[120^{\circ}\text{E} \sim 140^{\circ}\text{E}, 20^{\circ}\text{N} \sim 25^{\circ}\text{N}]$ ) is close to one. The region of high local  $Ro$  ( $Ro \geq 0.5$ ) occupies the subtropical upper-troposphere from the western to the central North Pacific ( $90^{\circ}\text{E} \sim 180^{\circ}$ ). In this region, the 900 hPa



geopotential height shows a meridionally relatively high belt (regions enclosed by 1030m contour in Fig. 3.1) beneath the upper-tropospheric high-Ro patch. The distribution of the local Ro and the lower-level geopotential height indicates that the circulation over the subtropical western and central North Pacific is under the thermally-driven regime and the subtropical high in this region may be controlled by the thermally-driven local Hadley cell.

To clarify the essence of the thermally-driven local Hadley cell in the western and central North Pacific, we compare the spatial relationship between the theoretical and observed local Hadley cell boundaries. The representation of the theoretical Hadley cell boundary is achieved by following the convective quasi-equilibrium theory (Chapter 2.3) to calculate the theoretical boundary of the thermally-driven Hadley cell over the North Pacific basin. The theoretical boundary (blue dashed line in Fig. 3.2) is close to the actual ridge line of the high (red solid line in Fig. 3.2) in the western and central Pacific west of 160°W. The alignment of the two ridges indicates the similarity between the observed circulation and the thermally-driven local Hadley cell over the western and central North Pacific.

The contribution from the tropical circulation could also be identified by the upper-tropospheric divergence and divergent wind (Fig. 3.2). The upper-tropospheric divergence field shows a meridional tripolar pattern with divergence in the Southern




Hemispheric tropics ( $15^{\circ}\text{S}\sim 0^{\circ}$ ) and midlatitudinal central Pacific ( $30^{\circ}\text{N}\sim 50^{\circ}\text{N}$ ) and convergence in the subtropical central Pacific ( $15^{\circ}\text{N}\sim 30^{\circ}\text{N}$ , shading in Fig. 3.2). The subtropical convergence coexists with the lower-tropospheric subsidence that is relevant to the subtropical high (orange shading in Fig. 1.1d) over the subtropical western and central North Pacific with a zonal-elongated structure. This coexistence suggests the importance of the upper-tropospheric convergence to the subtropical high. Associated with the divergence field, there are strong northward divergent winds from the Southern Hemispheric tropical western and central Pacific heading toward the subtropical central North Pacific. The northward divergent wind indicates the existence of the tropical meridional overturning circulation and its contribution to the subtropical subsidence. The agreement between these characteristics of the theoretical and observed Hadley cell thus supports the role of the thermally-driven local Hadley cell in this region.

In addition to the northward divergent flow from the tropics, Figure 3.2 also shows southward divergent flow over the midlatitudinal central Pacific. The direction of the upper-tropospheric divergent flow is distinct from the direction of the thermally-driven local Hadley cell, implying that processes other than tropical circulation exist. As shown in Figures 3.3a and 3.3b, this southward divergent wind is similar to the meridional ageostrophic wind. To identify the source of these northerlies in the central Pacific, we apply the time-mean horizontal ageostrophic wind decomposition (Chapter 2.4) to the

200 hPa wind field. The residual of the decomposition is relatively small compared to the total ageostrophic wind (Fig. 3.3c), suggesting the validity of this budget decomposition.

The decomposition demonstrates that the southward ageostrophic wind is mainly contributed by the mean flow advection terms (Fig. 3.3d and 3.3e) at the downstream region of the East Asian jet core. This means that the eastward acceleration at the jet exit region from the mean wind advection is balanced with the westward acceleration from Coriolis torque induced by the upper-tropospheric southward ageostrophic secondary circulation. This distribution is analogous to the concept of the geostrophic adjustment at the jet exit region.

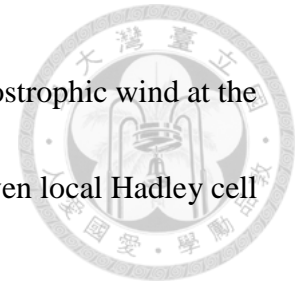
Considering the horizontal divergence from both zonal and meridional winds, the upper-tropospheric divergence budget over the subtropical central Pacific ( $[150^{\circ}\text{E}\sim 150^{\circ}\text{W}, 15^{\circ}\text{N}\sim 30^{\circ}\text{N}]$ ; Fig. 3.4) further suggests a dominant role of this meridional circulation from geostrophic adjustment. The first and second terms in the decomposition shown in Figure 3.4 (the third and fourth bars in Fig. 3.4) are the time-mean divergence from zonal (the first term in the second equation in ( 2.4 )) and meridional (the first term in the first equation in ( 2.4 )) secondary circulation, respectively. The effects of the eddy momentum flux divergence on both the zonal and meridional ageostrophic wind divergence are combined into the third term in the decomposition (the fifth bar in Fig. 3.4). Even though there is an overestimation of the



convergence from the ageostrophic wind (comparing the two leftmost columns in Fig. 3.4), the convergence from the mean meridional secondary circulation still contributes about 83% of the total ageostrophic convergence, while the eddy momentum flux divergence term contributes only about 14%. This minor role of eddies is also seen in Figure 3.3f in which the eddy-induced meridional ageostrophic wind is relatively weak in the subtropical central Pacific. These results from the budget decomposition reveal the importance of the East Asian jet to the upper-tropospheric convergence.

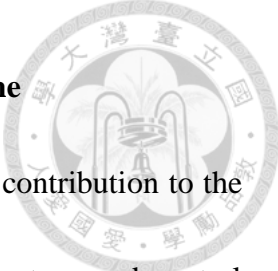
The intensity of the East Asian jet could be treated as a consequence of the tropical heating. Based on the concept introduced in Chapter 2.2 and the definition of local  $R_o$ , our analysis of local  $R_o$  implies that the mean angular momentum transport from the thermally-driven local Hadley cell is important to the strength of the jet over the western and central Pacific. Although some of the previous studies have shown that the jet in the North Pacific basin in winter is a combined effect of both the midlatitude baroclinic eddies and the mean momentum transport from the Hadley cell (Lee & Kim, 2003; Li & Wettstein, 2012), many of the others have suggested that the tropical heating is relevant to the intensity and the longitudinal extent of the jet in the North Pacific basin (Chan et al., 2020; Lau & Boyle, 1987; Li & Wettstein, 2012) and the downstream circulation in winter (Moore et al., 2010; Ryoo et al., 2013). Stronger tropical heating leads to stronger jet and more zonal-elongated downstream inertial advection. Due to this relationship

between the tropical heating and the jet, the jet intensity and the ageostrophic wind at the jet exit region are regarded as an indirect effect of the thermally-driven local Hadley cell in the subtropical central Pacific.



Combining the view of the Hadley cell's indirect effect with its direct subsidence from the tropics, the zonal-elongated upper-tropospheric convergence and lower-tropospheric subsidence over the western and central North Pacific are the results of the thermally-driven local Hadley cell. The zonal-elongated subsidence further leads to the strong (weak) 900 hPa anticyclonic shear (curvature) vorticity in this region (Fig. 3.5b, 3.5a). Thus, the subtropical high performs a belt-like structure rather than the closed loop as in the eastern Pacific, which has stronger curvature vorticity (Fig. 3.5a). This geometric feature implies that the description of the Sarachik inquiry about the subtropical high in winter needs to be reconsidered and modified. In the western and central Pacific, the region traditionally thought of as a weak subtropical high in winter, the strong anticyclonic shear vorticity in our analysis manifests the existence of a strong subtropical high belt in this region. The examination of the theoretical and actual local Hadley cell and the contribution from midlatitude geostrophic adjustment at the jet exit region suggest the direct and indirect control of the thermally-driven local Hadley cell to the zonal-elongated high belt.

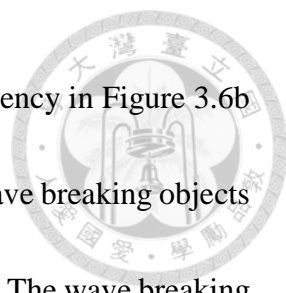
### 3.2 The Influence of Rossby Wave Breaking on the Anticyclone



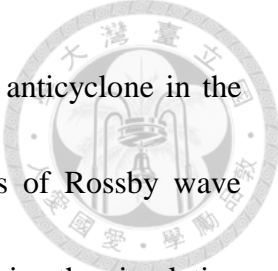
The results in Chapter 3.1 suggest that the eddies have a minor contribution to the upper-tropospheric convergence and the subtropical high in the western and central Pacific. Our next goal is to clarify the role of Rossby waves and wave breaking in the wintertime subtropical high as suggested by recent studies (Aemisegger et al., 2021; Ryoo et al., 2013). The potential of the Rossby wave breaking influencing the subtropical high in winter could be implied by the background field of the upper-troposphere in the North Pacific basin. As described in Chapter 2.2, the local  $Ro$  over the eddy-mediated circulation deviates from one. Figure 3.1 demonstrates that the local  $Ro$  over the closed anticyclone in the eastern Pacific (thick green contour) is close to zero. This implies a potential role of eddies in influencing the upper-tropospheric momentum balance and the convergence in this region.

The characteristics of Rossby waves also suggest this potential in the eastern Pacific. Based on previous literature about the prevalence of Rossby wave breaking, the weaker the jet and its associated weaker PV gradient lead to the higher occurrence of Rossby wave breaking due to the intrinsic properties of Rossby waves (Martius et al., 2007; Postel & Hitchman, 1999). Figure 3.6a demonstrates that both the background jet strength and PV gradient are weak in the east, suggesting a weaker waveguide of Rossby wave and thus a higher wave breaking frequency. The actual anticyclonic Rossby wave breaking





frequency is shown as shading in Figure 3.6b. We note that the frequency in Figure 3.6b denotes the percentage of the days detected as anticyclonic Rossby wave breaking objects on any isentropes spanning from 310K to 350K over the 18-year DJF. The wave breaking day is only counted once even if the wave breaking occurs on multiple isentropes. Being consistent with the background information of the waveguide, the actual wave breaking frequency is also concentrated in the eastern Pacific in which the PV gradient is relatively weak. The more zonal-directed WAF in the western and central Pacific also indicates that Rossby waves propagate along with the jet in the west and amplify and break in the east (arrow in Fig. 3.6b). It is noteworthy to mention that previous studies have shown the helpfulness of the westerly over the tropical eastern Pacific, called the “westerly duct”, for the southward propagating Rossby waves and the associated wave breaking (Waugh & Polvani, 2000; Webster & Holton, 1982). When the westerly duct is stronger, more waves propagate toward the tropical eastern Pacific and thus more Rossby wave breaking events in the subtropical eastern Pacific may occur. Our result also supports this feature as shown by the southward WAF in Figure 3.6b. This westerly duct thus provides a channel for midlatitude Rossby waves affecting the subtropical regions in the eastern North Pacific. Overall, the results from both the background field and the preference for Rossby wave breaking suggest the potential influence of Rossby wave breaking on the anticyclone with stronger curvature vorticity in the eastern Pacific.

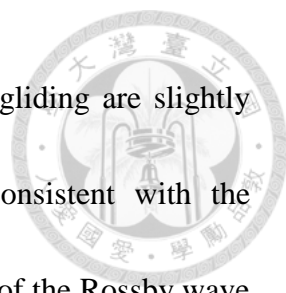


To clarify the processes of how the wave breaking affects the anticyclone in the eastern Pacific, we applied a case study and a composite analysis of Rossby wave breaking days in the North Pacific basin. For the case study, we examine the circulation of an arbitrary day of 340K anticyclonic wave breaking event (7<sup>th</sup> Jan. 2000) selected by the PV folding algorithm described in Chapter 2.6. The upper-tropospheric PV shows the folding of isolines over the eastern Pacific (contour in Fig. 3.7a). The PV folding is associated with lower-tropospheric subsidence to its west, which induces the closed anticyclone further west (Fig. 3.7b). This spatial relationship is similar to the description of the anomalous circulation induced by the upper-tropospheric positive PV anomaly in Funatsu & Waugh (2008). The positive PV anomaly aloft leads to the upward tilted isentropes beneath it and hence subsidence gliding along with the tilted isentropes and the lower-tropospheric high adjustment to the west of the isentropic downgliding. We then examine whether this anomalous circulation is only a single case or the general feature in Rossby wave breaking days by the composite analysis of the anticyclonic Rossby wave breaking days on 340K and 320K isentropes. The composite considers all anticyclonic Rossby wave breaking days on which the centroid of wave breaking object locates within the North Pacific basin ( $[120^{\circ}\text{E}\sim 100^{\circ}\text{W}, 0^{\circ}\sim 90^{\circ}\text{N}]$ ). The circulation structure of the Rossby wave breaking object-centered composite (Fig. 3.8a and 3.8c) also agrees with the relationship between upper-tropospheric PV folding, lower-tropospheric

subsidence, and surface high anomalies as shown in the case study and previous literature.

This consistency suggests the generality of the circulation response we found in the case study.


However, to measure the climatological effect of the Rossby wave breaking on the anticyclone in the eastern Pacific, the occurrence and prevalent location of wave breaking events must be considered as well. Figures 3.8b and 3.8d show the occurrence of the wave breaking object centroid on 340K and 320K isentropes, respectively. Wave breaking frequencies on both isentropes are concentrated in the eastern Pacific though the preferred latitude of wave breaking on 320K isentrope is higher than the latitude of breaking on 340K isentrope which is due to the climatological location of 2PVU isoline (Wernli & Sprenger, 2007). Considering the anomalous circulation and the occurrence of anticyclonic Rossby wave breaking together, Figures 3.9a and 3.9b demonstrate the anomalous 900 hPa geopotential height composite of the wave breaking days in the North Pacific basin. Although the anomalous highs locate slightly different on 340K and 320K wave breaking days, wave breaking on both isentropes are associated with anomalous highs in the eastern Pacific which is analogous to our results of the case study and object-centered composite. The vertical cross-section of the anomalous circulation at the longitude of preference also suggests a subtropical anomalous vertical motion gliding downward along with the isentropes (Fig. 3.10) which is consistent with the description



in Funatsu & Waugh (2008). The latitudes of the isentropic downgliding are slightly different on 340K and 320K wave breaking days, which is consistent with the characteristics of the latitude of the anomalous highs. The influence of the Rossby wave breaking on the subtropical high could be further demonstrated by comparing the geometric structure of the circulation in the non-Rossby wave breaking days and its climatology. The non-Rossby wave breaking days composite (Fig. 3.9c) shows that the anticyclone in the eastern Pacific is more zonal-elongated these days. This suggests the strengthening effect of the anticyclonic Rossby wave breaking on the closed anticyclone in the eastern Pacific.

The overall effect of Rossby wave breaking and the associated isentropic gliding on the time-mean circulation is identical to the concept of the wave-driven Stokes drift to the mean circulation. The breaking waves mix PV and masses between the extratropics and the tropics along with the isentropes on the synoptic time scale. The Rossby wave breaking induced PV mixing effect could flatten the background PV field, sustaining the weak meridional PV gradient in the eastern Pacific. This mass exchange induced Rossby wave breaking then provides the mass source of the time-mean subtropical subsidence.

The contribution from the transient waves to the seasonal averaged upper-tropospheric convergence is also examined by the ageostrophic wind budget decomposition as applied in Chapter 3.1 for the central North Pacific. Figure 3.11 shows




that the divergence of eddy momentum flux divergence contributes about 25% of the total 200 hPa ageostrophic wind convergence in the eastern North Pacific ([140°W~110°W, 20°N~40°N]). In contrast to the budget in the central North Pacific which is dominated by the time-mean meridional secondary circulation, the contributions from the three terms in the decomposition are more distributed and the contribution from transient eddies increases in the eastern Pacific. The decomposition in the east implies that the transient eddies affect the upper-tropospheric convergence with a considerable proportion.

In summary, the convergence budget decomposition in the eastern North Pacific indicates the positive contribution from transient eddies to the upper-tropospheric convergence. The case study and composite analysis also suggest that the anticyclonic Rossby wave breaking in the eastern North Pacific assist the formation of the closed anticyclone with stronger curvature vorticity in this region. The spatial distribution of the preference of wave breaking is further determined by the background weak westerlies and the associated weak Rossby wave waveguide. This eddy-mediated circulation is also consistent with the background information of local  $Ro \approx 1$  in the eastern Pacific.


### **3.3 The Unified Controlling Factor: Westerly Jet in the Pacific Basin**

Our results in Chapters 3.1 and 3.2 provide answers for the controlling factors of the wintertime North Pacific subtropical high in different regions. We suggest that the closed



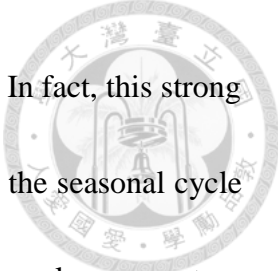
anticyclone with relatively strong curvature vorticity in the eastern Pacific is strengthened by the anticyclonic Rossby wave breaking. On the contrary, the thermally-driven local Hadley cell, directly and indirectly, controls the subtropical high belt in the western and central Pacific by affecting the strength and zonal extension of the East Asian jet. The jet strength and location could lead to the aforementioned different controlling factors in these two regions and thus different subtropical high regimes. The stronger jet in the western and central Pacific is associated with a steeper isentropic slope and higher meridional PV gradient (Fig. 3.12a) which further inhibits the anticyclonic Rossby wave breaking and the development of the closed anticyclone. The less wave breaking frequency reduces the effect of transient eddies on the momentum balance and therefore enhances the importance of the zonal-elongated thermally-driven circulation in the west. Additionally, the strong jet serves as a waveguide and sustains the eastward propagation of Rossby waves. These waves propagate to and break in the eastern Pacific, in which the jet strength and PV gradient are much weaker than those in the central Pacific (Fig. 3.12b), leading to a more eddy-driven circulation in the east. The breaking waves hence lead to the localized subsidence and the closed anticyclone with curvature vorticity in the eastern Pacific.

The differences in the subtropical high between west and east that are arisen from the jet are also evident in the geometric characteristics represented by the vorticity type



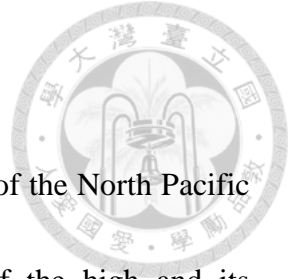
in the North Pacific basin. As concluded in the previous section, the strong shear vorticity-dominated high belt in the west (Fig. 3.5b) is the result of the zonal-elongated jet in the western and central Pacific. The relatively strong curvature vorticity-involved closed anticyclone in the east (Fig. 3.5a) is attributed to the anticyclonic Rossby wave breaking under the weak PV gradient in the eastern Pacific. The different vorticity types between west and east suggest the different regimes of the North Pacific subtropical high. Considering the two subtropical high regimes together, the total vorticity suggests the strong subtropical anticyclonic circulation in the North Pacific basin in winter. This is referred to the reconsideration of the Sarachik inquiry mentioned in Chapter 3.1. That is, the subtropical high in the central Pacific is strong in winter but presents as the high belt with strong shear vorticity. This also disentangles the paradox of weak wintertime subtropical high in the central Pacific.

In summary, the relationship between the jet, the associated dynamical constraint, and its role as the Rossby wave waveguide implies that the jet could be interpreted as a unified controlling factor of the North Pacific subtropical high in winter. Specifically, on one hand, the strength of the jet determines the prevalence of Rossby wave breaking and hence the relative importance of the eddies to the circulation; on the other hand, the zonal extension of the jet controls the geometric structure of the North Pacific subtropical high. The zonal-elongated East Asian jet in the western and central Pacific further leads to the



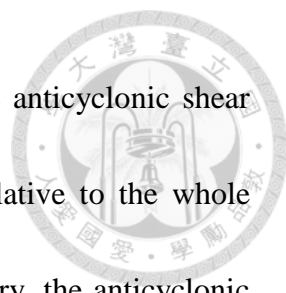
subtropical high belt with strong shear vorticity in the central Pacific. In fact, this strong anticyclonic shear vorticity in winter is also the strongest throughout the seasonal cycle (Fig. 3.5d). Since the jet is influenced by the tropical heating through angular momentum transport, the strongest Hadley cell throughout the seasonal cycle may play a role in affecting the seasonal evolution of the zonal-elongated subtropical high. To clarify the idea of the jet-mediated subtropical high and its relationship with the Hadley cell, we then further examine this hypothesis in seasons with different tropical heating, especially for winter-to-spring transition.





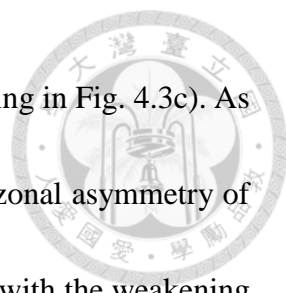
#### 4. The Transition from Winter to Spring

To verify our hypothesis of the jet-mediated controlling factor of the North Pacific subtropical high in winter, we analyze the seasonal transition of the high and its relationship with the evolution of the proposed perspective. Nigam & Chan (2009) shows that the most robust signature in the seasonal cycle of the North Pacific subtropical high is the increase of the surface high from winter to summer in the midlatitudinal ocean and is due to the change in the storm track. However, as introduced in Chapter 1, their Figure 4 also demonstrates that the strength of the high in the subtropical central Pacific peaks in April, rather than in July. Even though the magnitude of the change in the sea level pressure is relatively small during this period compared to the differences between winter and summer in the midlatitudes, this feature in the subtropical central Pacific still indicates the existence of a seasonal transition other than the winter-to-summer one. Our examination of the 900 hPa geopotential height seasonal cycle supports that this subtropical evolution could be seen as a westward expansion of the closed anticyclone from January to April (comparing the thick black contour in Fig. 1.1d and 1.1e). The expansion of the closed anticyclone further suggests a change in the circulation geometric structure in the subtropical central Pacific. Therefore, we examine the seasonal cycle of the area-averaged 900 hPa shear and curvature vorticity over the anticyclonic region in the subtropical central North Pacific (regions of  $\bar{\zeta} < 0$  in

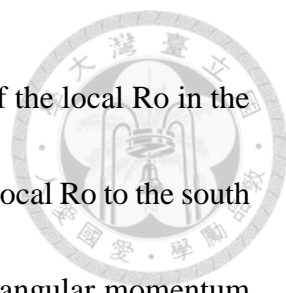


[160°E~160°W, 10°N~60°N]). Figure 4.1b displays a drop in the anticyclonic shear vorticity from January to April with the most abrupt decrease relative to the whole seasonal evolution occurring in February and March. On the contrary, the anticyclonic curvature vorticity rapidly strengthens in this time interval (Fig. 4.1a). These features are more clearly demonstrated with the help of the vorticity tendencies (pink lines in Fig. 4.1a and 4.1b) that show a large magnitude in February and March compared with other seasons, especially for shear vorticity. These evolutions imply the closed anticyclone expansion seen in Figures 1.1d and 1.1e. Furthermore, the timing is perhaps earlier than what one may expect if the abrupt westward expansion is linked with the summer monsoon onset. This indicates mechanisms other than South Asian and/or American monsoon should involve in this winter-to-spring abrupt transition.

The mechanism of the abrupt change in the North Pacific subtropical high is examined by the differences in the circulation between April and January. The change of the 900 hPa geopotential height shows an increase in the high in the extratropical central Pacific, leading to a more curved circulation (contour in Fig. 4.2). This increase of the high in the midlatitudes is associated with the strengthened lower-tropospheric subsidence (convection) at its east (west, shading in Fig. 4.2) which further reduces the zonal-elongated structure seen in winter. The strengthened lower-tropospheric subsidence in the subtropical eastern central Pacific ([180°~140°W, 30°N~45°N]) coexists with the

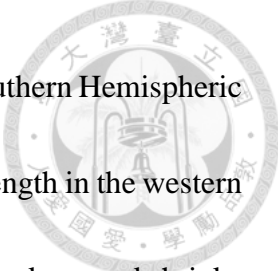


change in the upper-tropospheric convergence (comparing with shading in Fig. 4.3c). As shown in Figure 4.3, the change in the convergence stems from the zonal asymmetry of the differences in the meridional divergent wind which is associated with the weakening and westward retreating of the jet. Note that the most robust difference in the divergence is located at the regions of wintertime divergence but not convergence. Hence, this change should be recognized as a weakening of the upper-tropospheric divergence at the latitude north of the wintertime jet core. Figure 4.4 further demonstrates that the change in the convergence in this region is dominated by the weakening of the meridional secondary circulation at the jet exit region (the inertial advective  $\bar{v}_a$ ) in winter. This term contributes about four-fifths of the decreasing ageostrophic wind divergence in the eastern central Pacific. Since we focus on the circulation evolution in the eastern central Pacific, the divergence change is mainly attributed to the change in the secondary circulation but not the direct divergent wind from the local Hadley cell which may be important in the western Pacific (arrows in the subtropical North Pacific in Fig. 4.3c). The budget decomposition suggests the relevant role of the change in the jet and the associated inertial advective wind at the jet exit region in the winter-to-spring transition. The role of the jet in controlling the evolution of the subtropical high is consistent with our interpretation of the jet in the wintertime circulation as well.



The weakening of the jet is also implied by the rapid decrease of the local Ro in the subtropical western and central Pacific (Fig. 4.1c). The change in the local Ro to the south of the jet core indicates a weaker thermally-driven Hadley cell, less angular momentum transport from tropical heating, and thus the weaker subtropical jet. The timing of the subtropical Ro reduction is in good agreement with the evolution of the geometric features of the subtropical high (comparing Fig. 4.1c and 4.1b). Considering the role of the jet in the zonal-elongated subtropical high belt in winter, these coexisting transitions further suggest the importance of the weakened jet which is attributed to the less thermally-driven background.

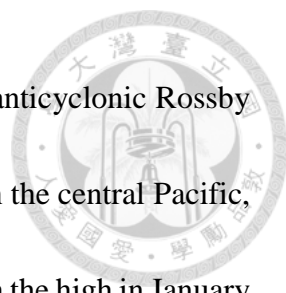
Since the transitions of the dynamical constraint and the jet strength are related to the evolution of the thermally-driven Hadley cell, we thus examine the seasonal cycle of tropical heating. The upper-tropospheric divergence in winter shows that most of the tropical overturning circulation diverges from the Southern Hemispheric tropics (Fig. 3.2). Therefore, we only consider the evolution of the Southern Hemispheric tropical heating in the following analysis. The heating is quantified by the apparent heat source, Q1, introduced in Yanai et al. (1973) that could represent the atmospheric heating. To calculate Q1 from the daily mean reanalysis data, we follow the formulation of eq. 1 and 2 in Hsu & Li (2011). The calculated Q1 on each isobaric level is then vertically integrated from the surface to 70 hPa to represent the total diabatic heating in the tropical



troposphere. The seasonal cycle of the column-integrated Q1 in the Southern Hemispheric tropics (meridionally averaged over  $20^{\circ}\text{S}\sim 0^{\circ}$ ) shows a maximum strength in the western and central Pacific in winter (Fig. 4.5). This heating maximum then weakens and shrinks from January to April. The evolution of the column-integrated Q1 is consistent with the local Ro transition in the subtropical central North Pacific. This further implies that the weakening of the Southern Hemispheric tropical heating is influential to the weakening of the subtropical jet and the associated zonal-elongated ageostrophic wind divergence from winter to spring.

In addition, we examine the effect of anticyclonic Rossby wave breaking on the rapid westward expansion of the anticyclone from January to April. The background information from the jet weakening suggests increasing Rossby wave breaking frequency and its potential for influencing this winter-to-spring transition. Indeed, Figure 4.6 shows that the anticyclonic Rossby wave breaking frequency increases from January to April, especially on 340K and 350K isentropes (lower panel in Fig. 4.6c). The wave breaking frequency also increases the most over the eastern central Pacific where the strongest upper-tropospheric convergence develops. This increasing wave breaking frequency is consistent with the expectation from the weakened jet and the associated waveguide.

However, the divergence budget decomposition in the eastern central Pacific suggests that the contribution from eddy momentum flux divergence is negligible to the



seasonal transition (Fig. 4.4). As shown in Figure 4.7, although the anticyclonic Rossby wave breaking on 340K isentrope could induce an anomalous high in the central Pacific, the strength of the wave breaking-induced high is weaker in April than the high in January. The weaker anomalous high leads to the minor role of the change in eddy term in the upper-tropospheric convergence despite the higher wave breaking frequency in April. Further examination is needed to clarify the reason for the weaker wave breaking-induced high. Nevertheless, the difference in the anomalous high between April and January still provides a clue for the inconsistency between the higher wave breaking frequency and the minor effect of the eddy term on the convergence in April in the eastern central Pacific.

In summary, the closed anticyclone with stronger curvature vorticity in the eastern Pacific shows a rapid westward expansion from January to April, which is distinct from the winter-to-summer evolution mentioned in previous studies. Our results suggest that this abrupt change is related to the weakening and westward retreating of the jet in the North Pacific basin from winter to spring which is attributed to the weakening of the Southern Hemispheric tropical heating. The weakened jet further reduces the ageostrophic northerlies at the wintertime jet exit region and thus increases the zonal asymmetry of the convergence and the lower-tropospheric curvature vorticity. Most importantly, this seasonal transition of the North Pacific subtropical high is regarded as

an application of the jet-mediated controlling factor concluded from the analysis of the wintertime subtropical high.




## 5. Conclusion and Discussion

The controlling factor of the North Pacific subtropical high in winter and its transition to spring is relatively less understood in contrast to its summertime counterpart.

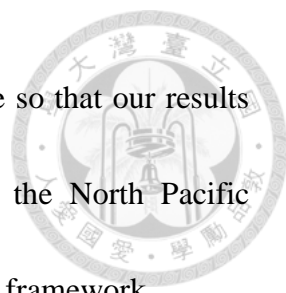
This study thus provides a comprehensive view of the formation mechanism of the climatological subtropical circulation in winter and winter-to-spring transition. Our results suggest a jet-mediated perspective of the controlling factor of the North Pacific subtropical high in the seasons we are interested in. For the wintertime circulation, the jet determines the circulation regime as summarized in Figure 5.1. The weak westerlies lead to an eddy-mediated circulation in the eastern Pacific, where the anticyclonic Rossby wave breaking strengthens the closed anticyclone. On the other hand, the jet is seen to suppress the wave breaking in the western and central Pacific, leading to a more thermally-driven background. The thermally-driven local Hadley cell originating from the Southern Hemispheric tropics then, directly and indirectly, controls the subtropical high in the west by its direct subsidence and its indirect effect on the geostrophic adjustment at the jet exit region, respectively. The zonal-elongated convergence from the tropics and the midlatitudes thus results in the subtropical high belt in the western and central Pacific in winter. The wintertime North Pacific subtropical high is hence separated into the shear vorticity-dominated high belt regime in the west and the more curvature vorticity-involved closed anticyclone regime in the east. For the winter-to-spring





transition of the North Pacific subtropical high, the relatively rapid westward expansion of the anticyclone can be partially attributed to the seasonal evolution of the Southern Hemispheric tropical heating. The decreasing tropical heating reduces the jet strength and the zonal-elongated structure in the subtropical central North Pacific. This seasonal transition further suggests the unified role of the jet in controlling the North Pacific subtropical high in winter and spring.

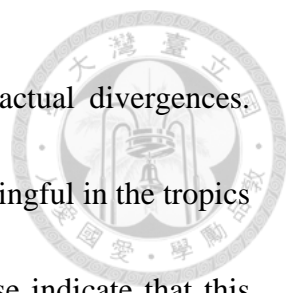
The concept of the relationship between the meridional overturning circulation, jet, and Rossby wave breaking in our results is similar to the zonal mean framework of the general circulation (Schneider, 2006; Vallis, 2017). However, our results emphasize the zonal asymmetry of the jet in the North Pacific basin. Rossby waves propagate along with the jet and break more in the zonal direction, while the waves' behavior is focused on the meridional direction in the zonal mean framework. Hence, our results suggest a longitudinal hotspot for Rossby wave breaking and the extratropical-tropical interaction associated with it, which is not considered when the zonal average is applied. This implication for the hotspot of wave breaking is similar to the conclusion of previous studies about the westerly duct and wave breaking (Vaughan & Polvani, 2000; Webster & Holton, 1982). The concept of the longitudinal hotspot also indicates that the eddy-driven circulation in the zonal mean framework should be more relevant in the eastern and central Pacific rather than over the whole latitudinal band. Further effort will be taken to



link these two concepts of the general circulation on the basin scale so that our results could provide the answer to not only the controlling factors of the North Pacific subtropical high but also to the three-dimensional general circulation framework.


In terms of the seasonal transition, it is noteworthy to compare our findings with the results in Nigam & Chan (2009), which focus on the winter-to-summer evolution of the North Pacific subtropical high in the extratropics and the midlatitude storm track. In contrast to their results, our findings concluded from the weakened jet provide additional information on the evolving high from winter to spring, which is likely different from the winter-to-summer one as mentioned in Chapter 1. Focusing on the transition from January to April, although the importance of storm track abatement is unclear in Nigam & Chan (2009), the change in the jet is possibly related to the change in the storm track. In fact, the wintertime upper-tropospheric divergence north of the jet at the central Pacific co-locates with the location of the storm track in winter. This implies that the weakened divergence at the jet exit region seen in our winter-to-spring transition is linked to the storm track forcing in Nigam & Chan (2009). However, the effect of the storm track on the jet requires more examination in the future.

It should also be noted that the upper-tropospheric divergence budget based on ageostrophic wind has its limitation on the latitudinal extent and the accuracy of the actual divergence. Our budget decomposition assumes that the ageostrophic wind is

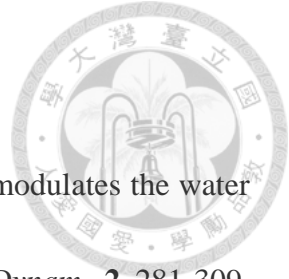


approximated to the divergent wind and contributes to all of the actual divergences. However, separating geostrophic and ageostrophic wind is less meaningful in the tropics and the divergent wind is not equal to the ageostrophic wind. These indicate that this decomposition is insufficient for the whole domain we are interested in and may result in an inaccurate estimation of the actual divergence. Furthermore, our current budget could not explicitly identify the contribution from the direct thermally-driven divergent flow introduced in Hsu & Plumb (2000). This reduces the merit of the ageostrophic wind budget decomposition. For these reasons, an actual divergence budget separating the contribution from the thermally-driven mean divergent wind and eddies is required for future diagnosis. This will help us to more precisely identify the importance of each physical process.

In addition, the contribution from high- and low-frequency eddies are not separated in our current budget decomposition. The eddy momentum flux divergence is not well linked to WAF as well. Therefore, decomposing eddy terms into different frequencies and linking them to WAF in the future will provide more information for understanding the details of contribution from Rossby wave breaking. Notwithstanding these limitations, the results from the current budget still imply the distinct role of the mean flow and eddies on the formation mechanism of the North Pacific subtropical high.



To clarify the causality between the seasonal transition of the tropical heating, the jet, the dynamical constraint, and the subtropical high, we are also conducting an idealized experiment of prescribed tropical heating. This experiment could support our hypothesis on the role of the jet in controlling the rapid winter-to-spring transition of the North Pacific subtropical high. Nevertheless, based on our current results, we regard the jet as a unified controlling factor of the subtropical high in the North Pacific basin. This point of view further suggests the centrality of the jet in the three-dimensional general circulation in a single ocean basin and provides a pathway for understanding the processes of extratropical-tropical interaction.



## References

- Aemisegger, F., and Coauthors, 2021: How Rossby wave breaking modulates the water cycle in the North Atlantic trade wind region. *Weather Clim. Dynam.*, **2**, 281-309.
- Chan, D., Y. Zhang, Q. Wu, and X. Dai, 2020: Quantifying the dynamics of the interannual variabilities of the wintertime East Asian Jet Core. *Climate Dynamics*, **54**, 2447-2463.
- Chen, P., M. P. Hoerling, and R. M. Dole, 2001: The Origin of the Subtropical Anticyclones. *Journal of the Atmospheric Sciences*, **58**, 1827-1835.
- Chen, T.-C., 2005: The Structure and Maintenance of Stationary Waves in the Winter Northern Hemisphere. *Journal of the Atmospheric Sciences*, **62**, 3637-3660.
- Cherchi, A., T. Ambrizzi, S. Behera, A. C. V. Freitas, Y. Morioka, and T. Zhou, 2018: The Response of Subtropical Highs to Climate Change. *Current Climate Change Reports*, **4**, 371-382.
- Dee, D. P., and Coauthors, 2011: The ERA-Interim reanalysis: configuration and performance of the data assimilation system. *Quarterly Journal of the Royal Meteorological Society*, **137**, 553-597.
- Emanuel, K. A., 1995: On Thermally Direct Circulations in Moist Atmospheres. *Journal of Atmospheric Sciences*, **52**, 1529-1534.



Funatsu, B. M., and D. W. Waugh, 2008: Connections between Potential Vorticity

Intrusions and Convection in the Eastern Tropical Pacific. *Journal of the*

*Atmospheric Sciences*, **65**, 987-1002.

Held, I. M., and A. Y. Hou, 1980: Nonlinear Axially Symmetric Circulations in a Nearly

Inviscid Atmosphere. *Journal of Atmospheric Sciences*, **37**, 515-533.

Held, I. M., M. Ting, and H. Wang, 2002: Northern Winter Stationary Waves: Theory

and Modeling. *Journal of Climate*, **15**, 2125-2144.

Homeyer, C. R., and K. P. Bowman, 2013: Rossby Wave Breaking and Transport

between the Tropics and Extratropics above the Subtropical Jet. *Journal of the*

*Atmospheric Sciences*, **70**, 607-626.

Hoskins, B. J., I. N. James, and G. H. White, 1983: The Shape, Propagation and Mean-

Flow Interaction of Large-Scale Weather Systems. *Journal of Atmospheric*

*Sciences*, **40**, 1595-1612.

Hsu, C. J., and R. A. Plumb, 2000: Nonaxisymmetric Thermally Driven Circulations and

Upper-Tropospheric Monsoon Dynamics. *Journal of the Atmospheric Sciences*,

**57**, 1255-1276.

Hsu, P.-C., and T. Li, 2011: Interactions between Boreal Summer Intraseasonal

Oscillations and Synoptic-Scale Disturbances over the Western North Pacific.



Part II: Apparent Heat and Moisture Sources and Eddy Momentum Transport.

*Journal of Climate*, **24**, 942-961.

Huffman, G. J., and Coauthors, 2001: Global Precipitation at One-Degree Daily

Resolution from Multisatellite Observations. *Journal of Hydrometeorology*, **2**, 36-

50.

Klein, S. A., D. L. Hartmann, and J. R. Norris, 1995: On the Relationships among Low-

Cloud Structure, Sea Surface Temperature, and Atmospheric Circulation in the

Summertime Northeast Pacific. *Journal of Climate*, **8**, 1140-1155.

Lau, K. M., and J. S. Boyle, 1987: Tropical and Extratropical Forcing of the Large-Scale

Circulation: A Diagnostic Study. *Monthly Weather Review*, **115**, 400-428.

Lee, S., and H.-k. Kim, 2003: The Dynamical Relationship between Subtropical and

Eddy-Driven Jets. *Journal of the Atmospheric Sciences*, **60**, 1490-1503.

Li, C., and J. J. Wettstein, 2012: Thermally Driven and Eddy-Driven Jet Variability in

Reanalysis. *Journal of Climate*, **25**, 1587-1596.

Li, W., L. Li, R. Fu, Y. Deng, and H. Wang, 2011: Changes to the North Atlantic

Subtropical High and Its Role in the Intensification of Summer Rainfall

Variability in the Southeastern United States. *Journal of Climate*, **24**, 1499-1506.

Lindzen, R. S., and A. V. Hou, 1988: Hadley Circulations for Zonally Averaged Heating

Centered off the Equator. *Journal of Atmospheric Sciences*, **45**, 2416-2427.



Liu, Y., G. Wu, and R. Ren, 2004: Relationship between the Subtropical Anticyclone and Diabatic Heating. *Journal of Climate*, **17**, 682-698.

Martius, O., C. Schwierz, and H. C. Davies, 2007: Breaking Waves at the Tropopause in the Wintertime Northern Hemisphere: Climatological Analyses of the Orientation and the Theoretical LC1/2 Classification. *Journal of the Atmospheric Sciences*, **64**, 2576-2592.

Moore, R. W., O. Martius, and T. Spengler, 2010: The Modulation of the Subtropical and Extratropical Atmosphere in the Pacific Basin in Response to the Madden–Julian Oscillation. *Monthly Weather Review*, **138**, 2761-2779.

Nie, J., W. R. Boos, and Z. Kuang, 2010: Observational Evaluation of a Convective Quasi-Equilibrium View of Monsoons. *Journal of Climate*, **23**, 4416-4428.

Nigam, S., and S. C. Chan, 2009: On the Summertime Strengthening of the Northern Hemisphere Pacific Sea Level Pressure Anticyclone. *Journal of Climate*, **22**, 1174-1192.

Postel, G. A., and M. H. Hitchman, 1999: A Climatology of Rossby Wave Breaking along the Subtropical Tropopause. *Journal of the Atmospheric Sciences*, **56**, 359-373.

Rodwell, M. J., and B. J. Hoskins, 2001: Subtropical Anticyclones and Summer Monsoons. *Journal of Climate*, **14**, 3192-3211.





Ryoo, J.-M., Y. Kaspi, D. W. Waugh, G. N. Kiladis, D. E. Waliser, E. J. Fetzer, and J.

Kim, 2013: Impact of Rossby Wave Breaking on U.S. West Coast Winter Precipitation during ENSO Events. *Journal of Climate*, **26**, 6360-6382.

Schneider, E. K., 1987: A Simplified Model of the Modified Hadley Circulation. *Journal of Atmospheric Sciences*, **44**, 3311-3328.

Schneider, T., 2006: The General Circulation of the Atmosphere. *Annual Review of Earth and Planetary Sciences*, **34**, 655-688.

Schneider, T., and S. Bordoni, 2008: Eddy-Mediated Regime Transitions in the Seasonal Cycle of a Hadley Circulation and Implications for Monsoon Dynamics. *Journal of the Atmospheric Sciences*, **65**, 915-934.

Seager, R., R. Murtugudde, N. Naik, A. Clement, N. Gordon, and J. Miller, 2003: Air–Sea Interaction and the Seasonal Cycle of the Subtropical Anticyclones. *Journal of Climate*, **16**, 1948-1966.

Shaw, T. A., and A. Voigt, 2016a: Understanding the Links between Subtropical and Extratropical Circulation Responses to Climate Change Using Aquaplanet Model Simulations. *Journal of Climate*, **29**, 6637-6657.

——, 2016b: What can moist thermodynamics tell us about circulation shifts in response to uniform warming? *Geophysical Research Letters*, **43**, 4566-4575.



Song, F., L. R. Leung, J. Lu, and L. Dong, 2018: Future Changes in Seasonality of the North Pacific and North Atlantic Subtropical Highs. *Geophysical Research Letters*, **45**, 11,959-911,968.

Sprenger, M., and Coauthors, 2017: Global Climatologies of Eulerian and Lagrangian Flow Features based on ERA-Interim. *Bulletin of the American Meteorological Society*, **98**, 1739-1748.

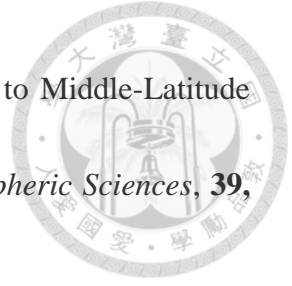
Takaya, K., and H. Nakamura, 2001: A Formulation of a Phase-Independent Wave-Activity Flux for Stationary and Migratory Quasigeostrophic Eddies on a Zonally Varying Basic Flow. *Journal of the Atmospheric Sciences*, **58**, 608-627.

Thorncroft, C. D., B. J. Hoskins, and M. E. McIntyre, 1993: Two paradigms of baroclinic-wave life-cycle behaviour. *Quarterly Journal of the Royal Meteorological Society*, **119**, 17-55.

Ting, M., 1994: Maintenance of Northern Summer Stationary Waves in a GCM. *Journal of Atmospheric Sciences*, **51**, 3286-3308.

Vallis, G. K., 2017: The Overturning Circulation: Hadley and Ferrel Cells. *Atmospheric and Oceanic Fluid Dynamics: Fundamentals and Large-Scale Circulation*, 2 ed., G. K. Vallis, Ed., Cambridge University Press, 511-538.

Waugh, D. W., and L. M. Polvani, 2000: Climatology of intrusions into the tropical upper troposphere. *Geophysical Research Letters*, **27**, 3857-3860.

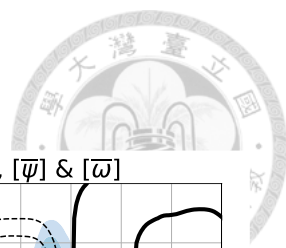


Webster, P. J., and J. R. Holton, 1982: Cross-Equatorial Response to Middle-Latitude Forcing in a Zonally Varying Basic State. *Journal of Atmospheric Sciences*, **39**, 722-733.

Wernli, H., and M. Sprenger, 2007: Identification and ERA-15 Climatology of Potential Vorticity Streamers and Cutoffs near the Extratropical Tropopause. *Journal of the Atmospheric Sciences*, **64**, 1569-1586.

Yanai, M., S. Esbensen, and J.-H. Chu, 1973: Determination of Bulk Properties of Tropical Cloud Clusters from Large-Scale Heat and Moisture Budgets. *Journal of Atmospheric Sciences*, **30**, 611-627.

Zhai, J., and W. Boos, 2015: Regime Transitions of Cross-Equatorial Hadley Circulations with Zonally Asymmetric Thermal Forcings. *Journal of the Atmospheric Sciences*, **72**, 3800-3818.



## Figures

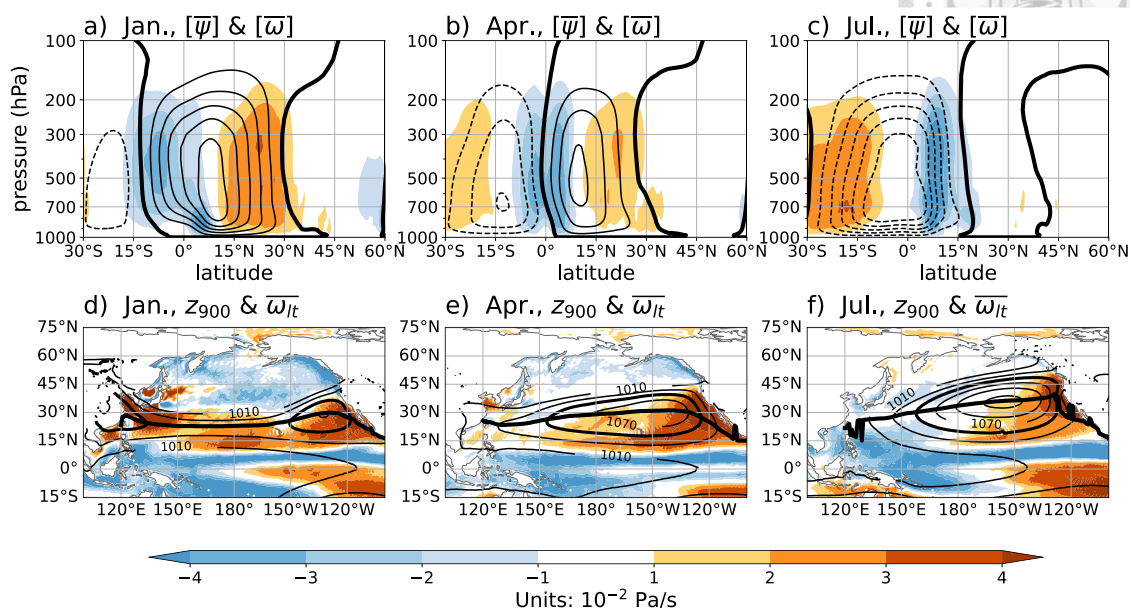


**Fig. 1.1** Climatology of **(top)** the globally zonal mean vertical structure of mass streamfunction (contour) and  $\omega$  (shading) and **(bottom)** 900 hPa geopotential height (contour; unit: m), lower-tropospheric  $\omega$  (shading), and high ridge (thick black line). The left, central, and right columns are January, April, and July, respectively. The contour interval in the top row is  $4 \times 10^{10}$  kg/s. The lower-tropospheric  $\omega$  in the bottom row is mass-weighted vertical averaged  $\omega$  from 700 to 900 hPa.

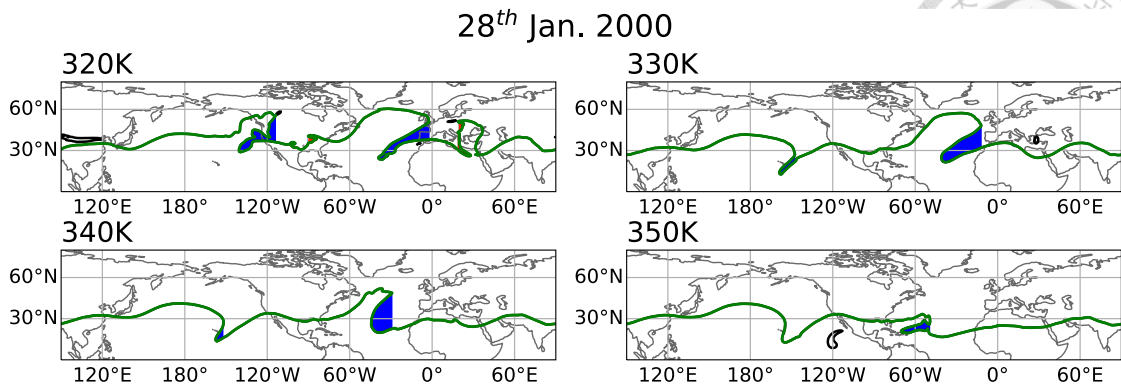


**Fig. 2.1** Illustration of the Rossby wave breaking identification algorithm. 2PVU isolines (green and black lines) and regions of stratospheric PV folding (color) on 28<sup>th</sup> Jan. 2000. The longest 2PVU isoline on each isentropic over the globe is marked as the green line. The blue (red) colored patches are regions of anticyclonic (cyclonic) Rossby wave breaking regions.

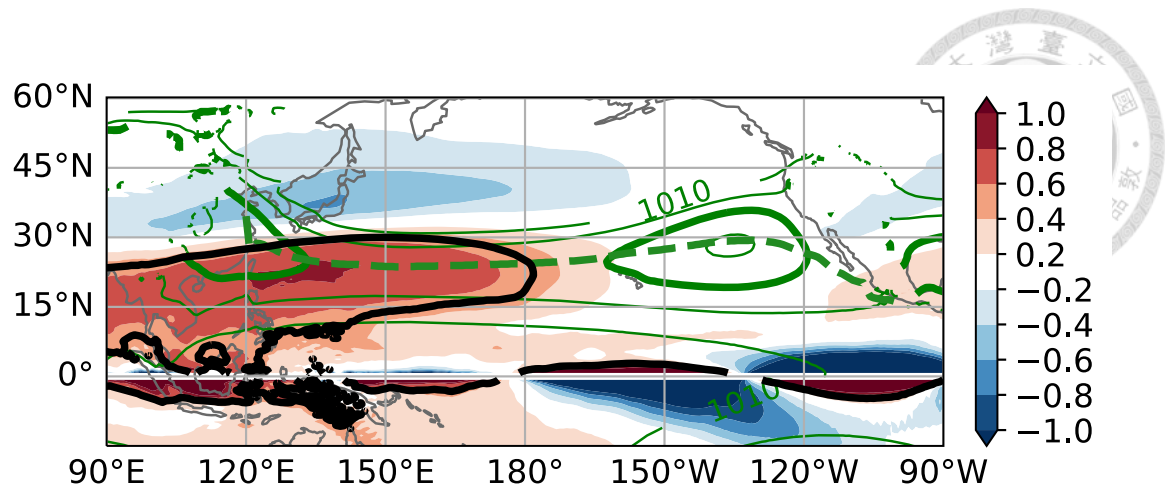


**Fig. 3.1** DJF climatology of 200 hPa local  $R_o$  (shading; unit: 1), 900 hPa geopotential height (green contour), and subtropical high ridge (green dashed line). The local  $R_o = 0.5$  isolines are shown as thick black lines to indicate the region of the thermally-driven regime. The contour interval of the geopotential high is 20m with thickened 1050m isolines.

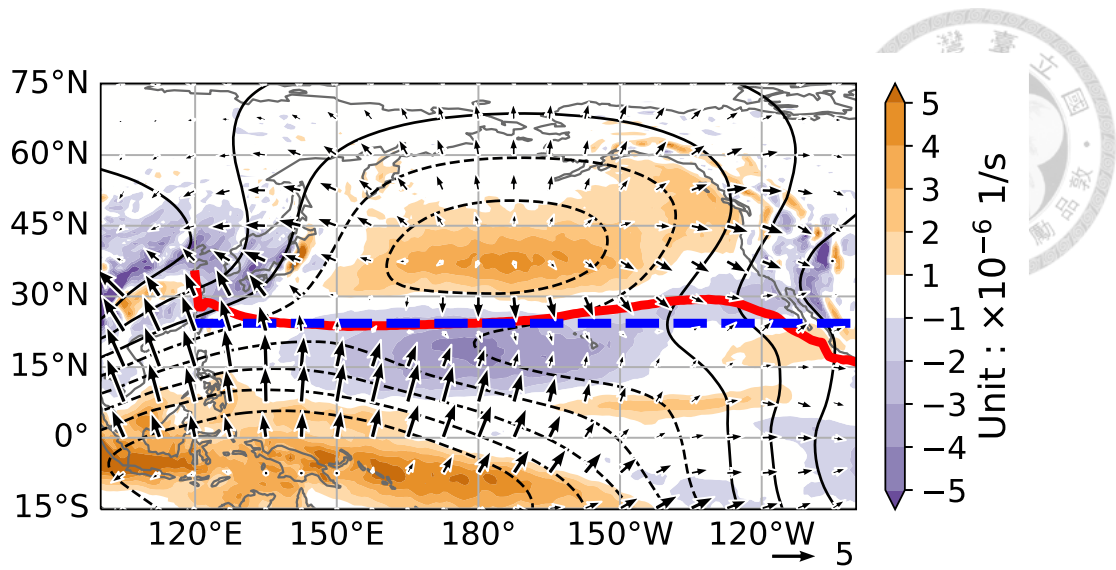


**Fig. 3.2** DJF climatology of 200 hPa divergence (shading), velocity potential (contour), divergent wind (arrow), and subtropical high ridge (thick red solid and blue dashed line) in the North Pacific basin. The contour interval of velocity potential is  $2 \times 10^6 \text{ m}^2/\text{s}$ . The unit of divergent wind is  $\text{m/s}$ . The red solid and blue dashed lines are the actual and theoretical ridge lines of zero surface zonal wind, respectively.

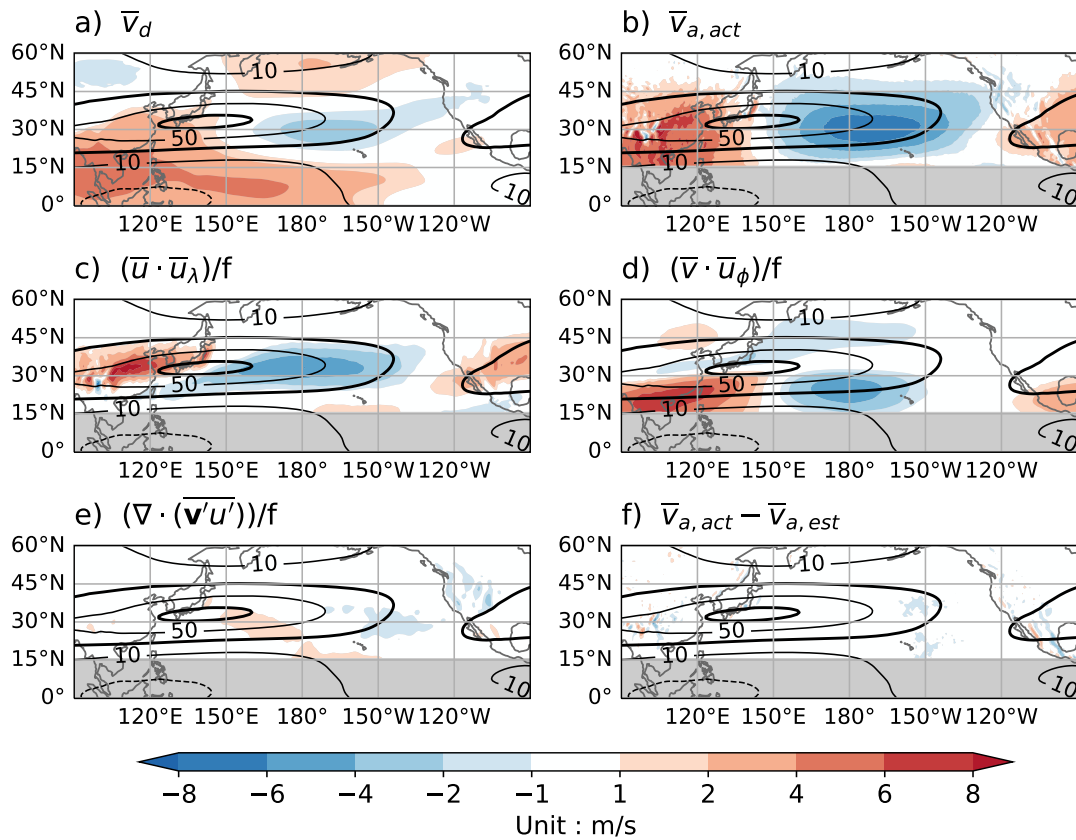


**Fig. 3.3** DJF climatology of 200 hPa meridional wind (shading) and zonal wind (contour; unit: m/s). The meridional winds in the upper row denote (a) actual divergent wind,  $\bar{v}_d$ , and (b) actual ageostrophic wind,  $\bar{v}_{a,act}$ . (c)-(e) are estimated ageostrophic wind,  $\bar{v}_{a,est}$ , by (c) zonal wind inertial advection,  $\bar{u} \cdot \partial \bar{u} / \partial \lambda \cdot (fa \cos \phi)^{-1}$ , (d) meridional wind inertial advection,  $\bar{v} \cdot \partial \bar{u} / \partial \phi \cdot (fa)^{-1}$ , and (e) transient eddy momentum flux divergence. (f) is the difference between  $\bar{v}_{a,act}$  and  $\bar{v}_{a,est}$ . The  $\bar{v}_{a,est}$  is the summation of (c)-(e). Due to the validity of quasi-geostrophic approximation, the region equatorward of  $15^\circ\text{N}$  is ignored and masked for the terms related to  $\bar{v}_d$ .



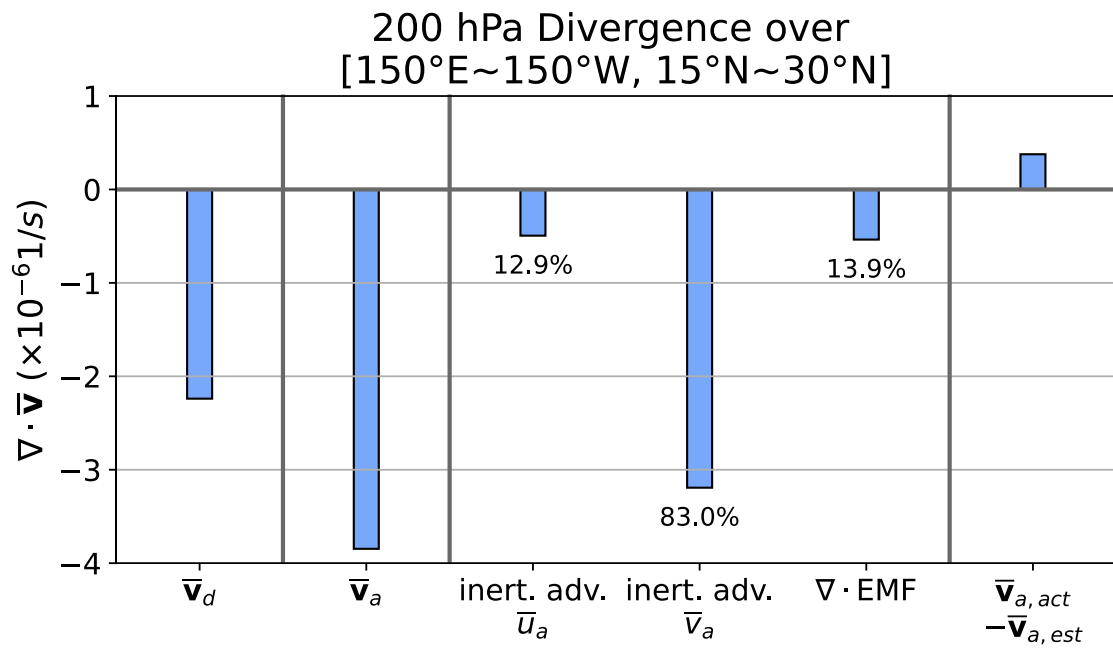


**Fig. 3.4** DJF climatology of 200 hPa divergence contributed by different terms in ageostrophic wind decomposition over the subtropical central Pacific ([150°E~150°W, 15°N~30°N]). The divergence considers both meridional and zonal directions. The three terms in the middle denote the zonal divergence of inertial advective  $\bar{u}_a$  ( $-(\bar{\mathbf{v}} \cdot \nabla)\bar{v}/f$ ), the meridional divergence of inertial advective  $\bar{v}_a$  ( $(\bar{\mathbf{v}} \cdot \nabla)\bar{u}/f$ ), and the horizontal divergence of eddy momentum flux divergence ( $\langle -\nabla \cdot (\bar{\mathbf{v}}'v')/f, \nabla \cdot (\bar{\mathbf{v}}'u')/f \rangle$ ), respectively. The numbers below the bars are the percentages of contribution from different terms to the total divergence of ageostrophic wind.

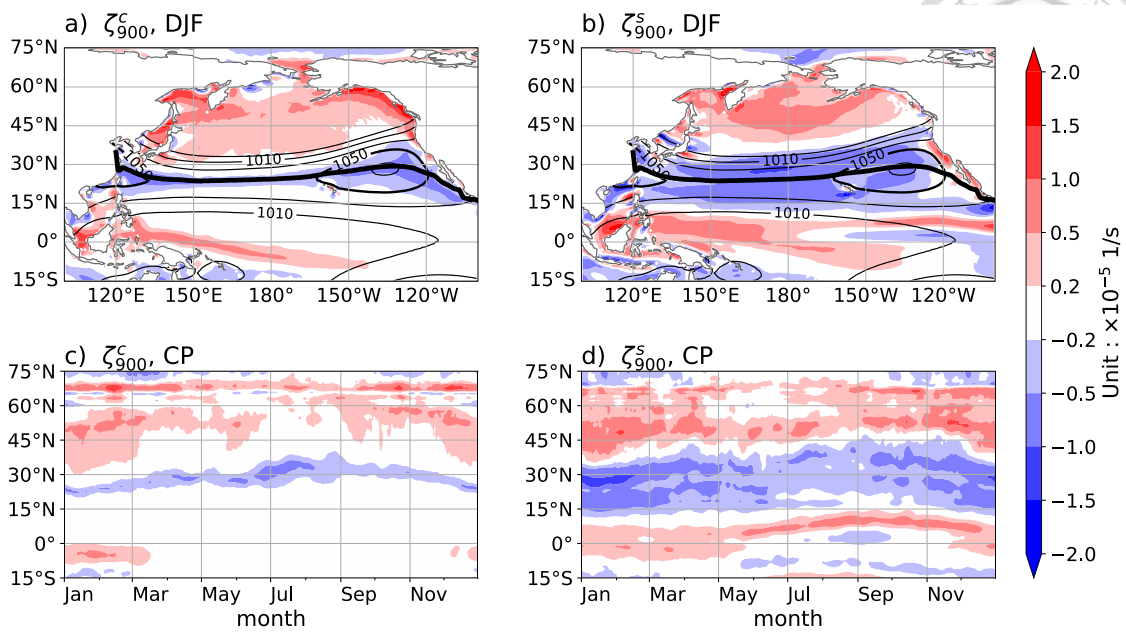


**Fig. 3.5** (upper) DJF climatology of 900 hPa (a) curvature and (b) shear vorticity (shading) and geopotential height (contour; unit: m). (bottom) The annual cycle of the  $\pm 5$ -day running mean zonal mean 900 hPa (c) curvature and (d) shear vorticity in the central Pacific sector ( $160^\circ\text{E}\sim 160^\circ\text{W}$ ).

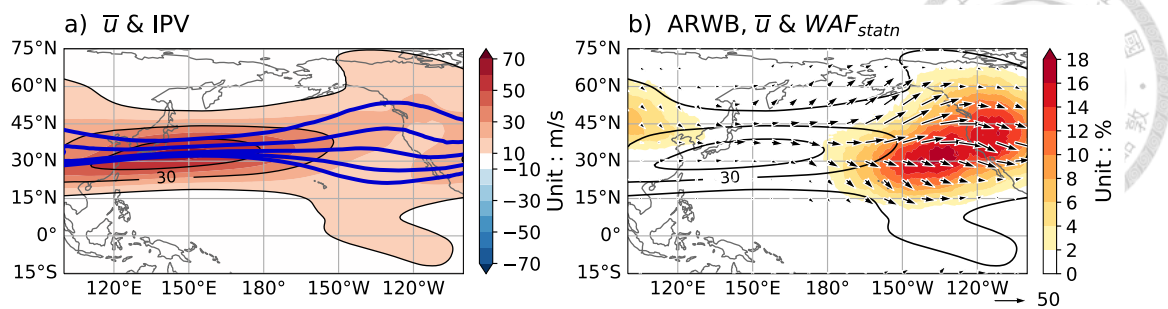


**Fig. 3.6** DJF climatology of the jet and Rossby wave waveguide. (a) 300 hPa zonal wind (shading) and 2PVU isolines on 310K to 350K isentropes (blue lines). (b) Anticyclonic Rossby wave breaking frequency summed over 310K to 350K (shading), 300 hPa zonal wind (contour), and stationary WAF (arrow).

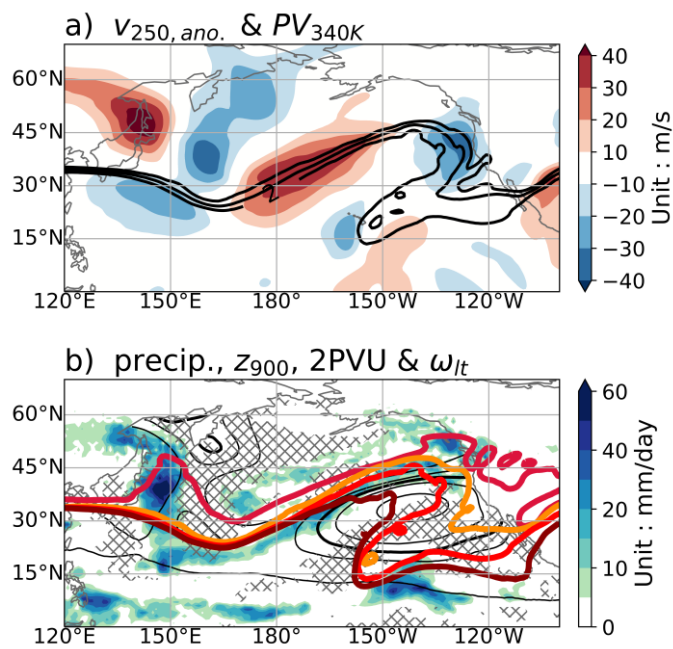


**Fig. 3.7** Weather map on 7<sup>th</sup> Jan. 2000. (a) 250 hPa anomalous meridional wind relative to DJF climatology (shading) and 340K PV (contour; 2, 3, and 4 PVU). (b) precipitation (shading), lower-tropospheric  $\omega$  ( $\omega_{lt}$ , grey crosses), 900 hPa geopotential height (contour), and 2PVU isolines on 320K – 340K isentropes (thick red lines). The  $\omega_{lt}$  is mass-weighted vertical averaged  $\omega$  from 500 to 700 hPa and only shown over the regions of  $\omega_{lt} \geq 0.04$  Pa/s. The contours of geopotential height start from 1030m with an interval of 40m and thickened 1090m contour. The 2PVU isolines on 320K – 340K isentropes with 10K intervals are in crimson, orange, red, and dark red, respectively.

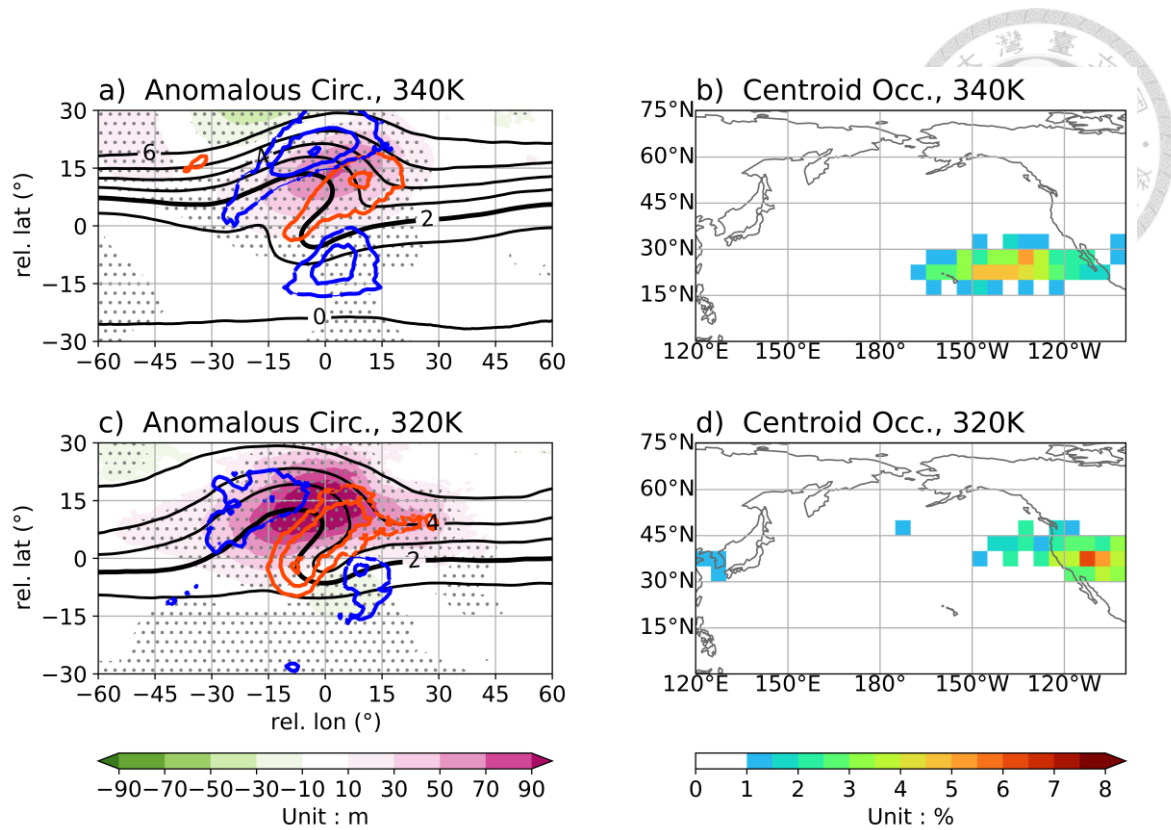


**Fig. 3.8** Anticyclonic Rossby wave breaking features on (**upper**) 340K and (**lower**) 320K isentropes over the North Pacific basin (120°E~100°W). (**left**) The Rossby wave breaking object-centered composite of anomalous 900 hPa geopotential height (shading), anomalous precipitation (blue contour), anomalous  $\omega_{lt}$  (orange contour), and actual PV (black contour; unit: PVU). Only the precipitation ( $\omega_{lt}$ ) anomalies larger than 1 mm/day (0.04 Pa/s) are shown with contour interval of 1.5 mm/day (0.04 Pa/s). The statistically significant ( $p=5\%$ ) anomalous geopotential height, precipitation, and  $\omega_{lt}$  are denoted by grey dots, thick blue, and thick orange contours, respectively. (**right**) two-dimensional histogram of the occurrence of anticyclonic Rossby wave breaking centroid within each  $5^\circ \times 5^\circ$  box over the North Pacific basin. The

summation of the values in colored regions is 100% of the anticyclonic Rossby

wave breaking days on each isentrope.



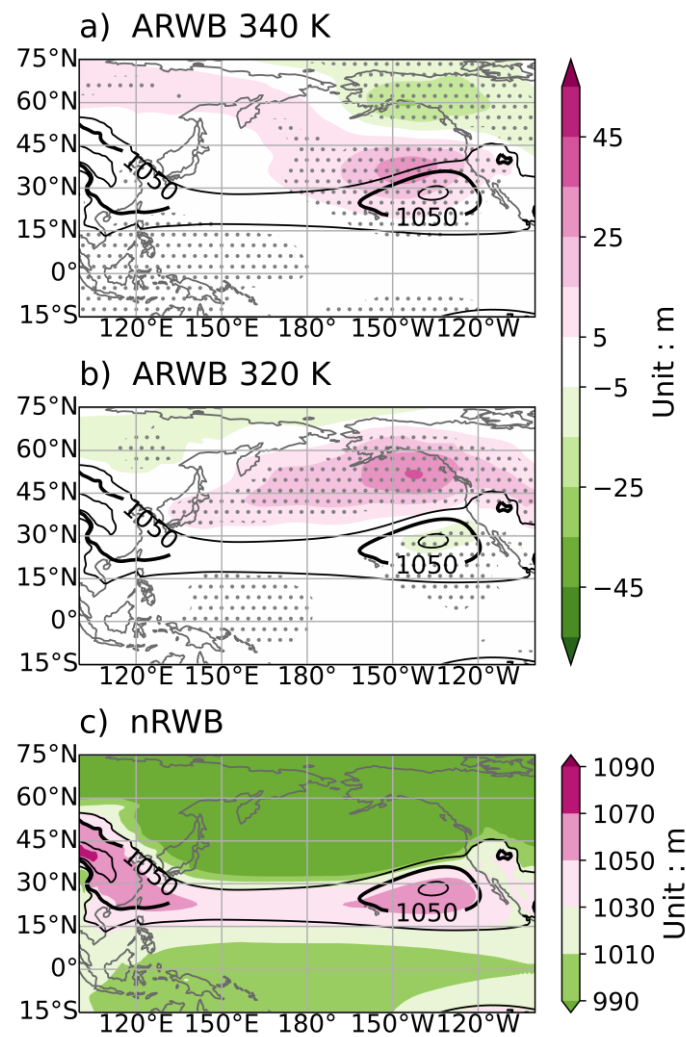


**Fig. 3.9** The composite of 900 hPa geopotential height on (a) 340K, (b) 320K anticyclonic Rossby wave breaking days, and (c) non-Rossby wave breaking days. The shading in (c) are the actual values while in (a) and (b) are anomalies relative to climatology (contour) with grey dots for statistical significance ( $p=5\%$ ).

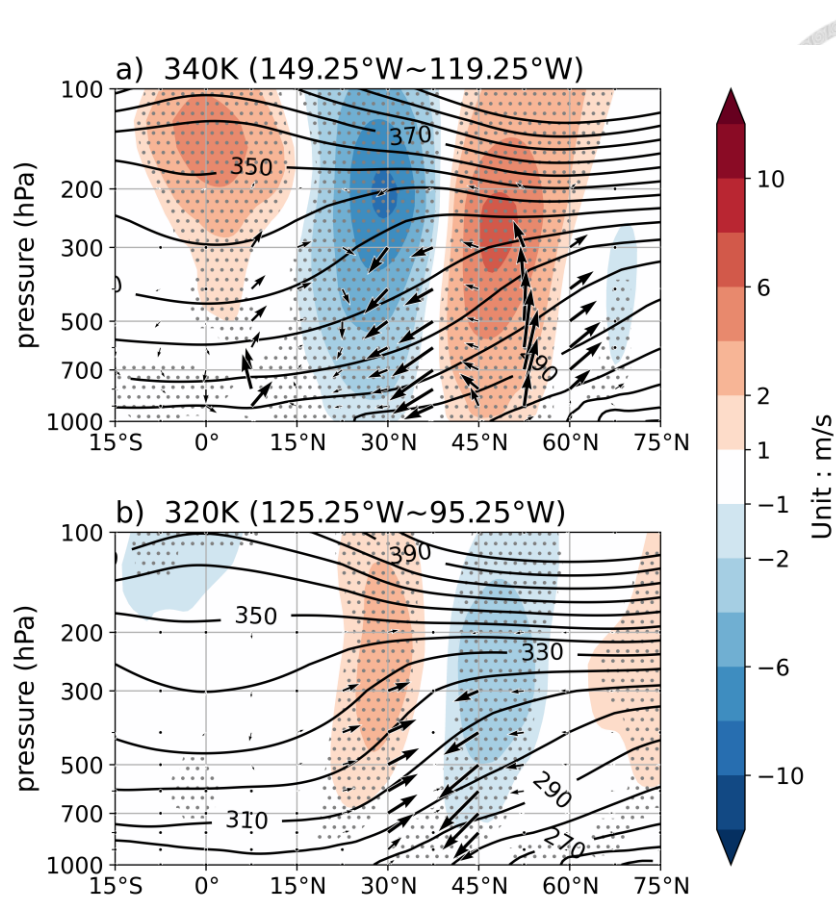


**Fig. 3.10** The composite of zonal mean anomalous zonal wind (shading), anomalous vertical circulation ( $\langle v, \omega \rangle$ , arrow), and actual isentropes (contour) on (a) 340K and (b) 320K anticyclonic Rossby wave breaking days in the chosen sectors. The sector for the certain isentrope is a  $30^\circ$  wide band centered at the longitude of the maximum anticyclonic Rossby wave breaking frequency on the given isentrope. The grey dots denote the statistically significant ( $p=5\%$ ) anomalous zonal wind.



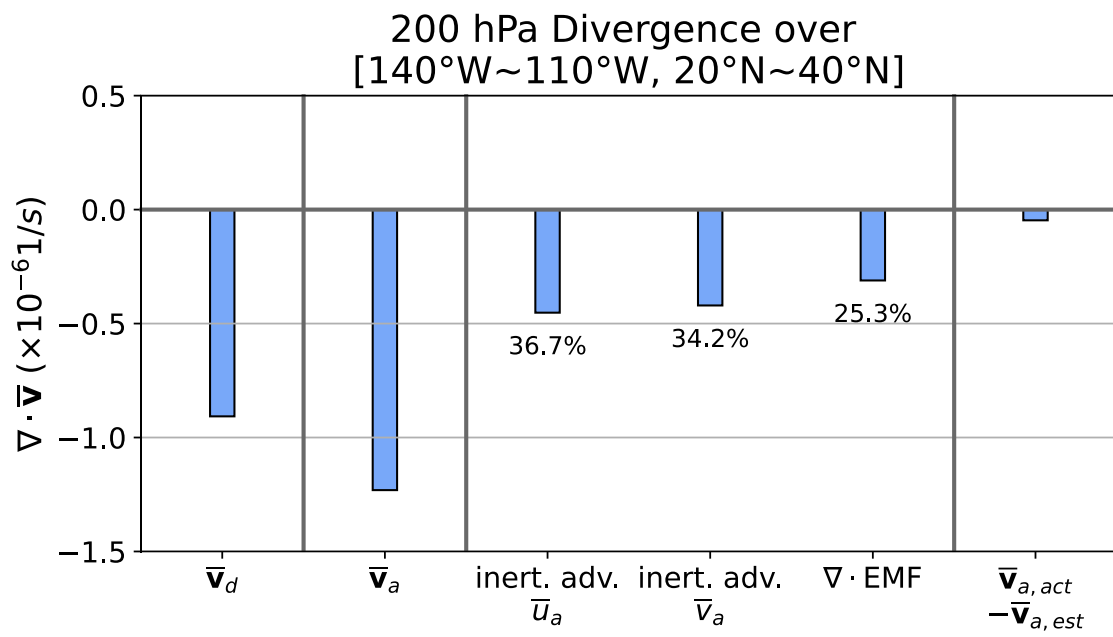


**Fig. 3.11** As in **Fig. 3.4**, but for divergence over the subtropical eastern Pacific.

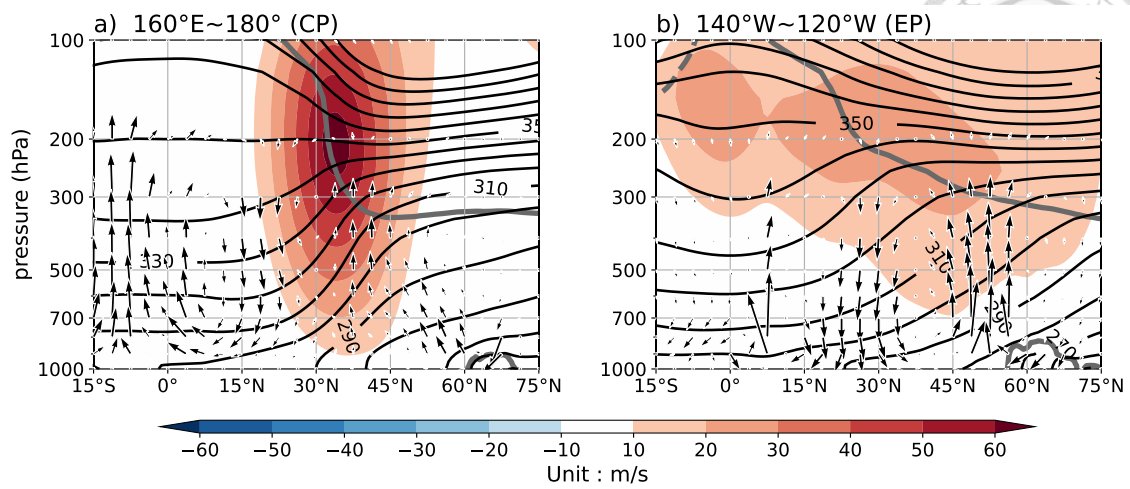


**Fig. 3.12** DJF climatology of zonal wind (shading), isentropes (black contour; unit: K), 2PVU isoline (thick grey line), and meridional overturning circulation ( $\langle \bar{v}_d, \bar{\omega} \rangle$ , arrow) zonally averaged in (a) 160°E~180° and (b) 140°W~120°W.

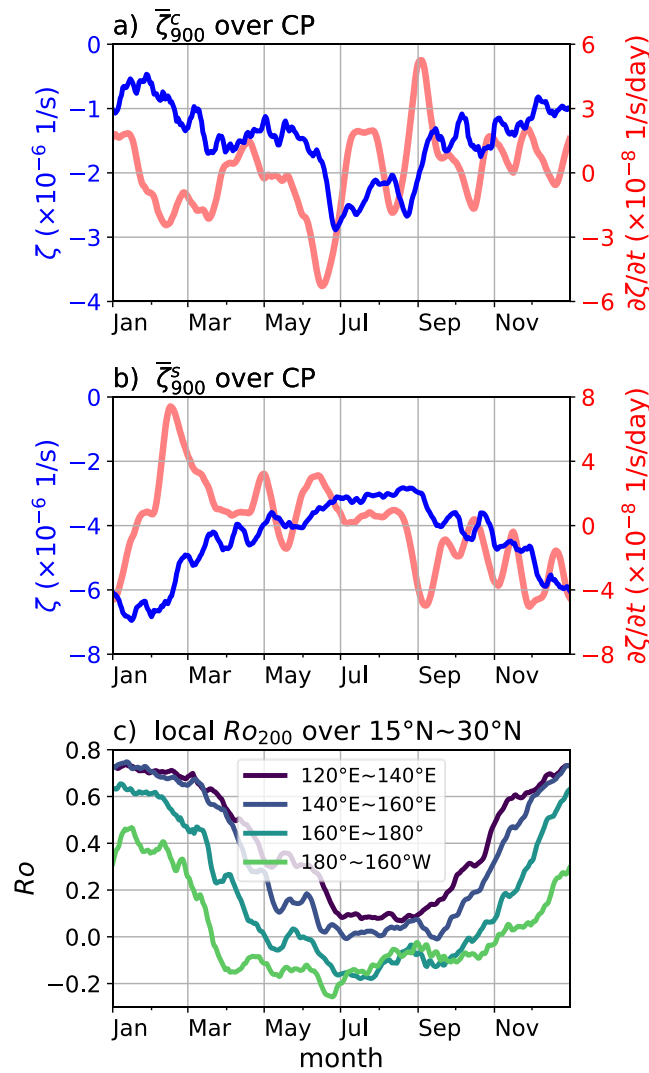


**Fig. 4.1** Seasonal evolution of the circulation features in the North Pacific basin. (a)  $\pm 5$ -days running mean of curvature vorticity averaged over anticyclonic regions in the central Pacific (blue) and its  $\pm 15$ -days running tendency (pink). (b), same as (a) but for shear vorticity. (c) 200 hPa local  $Ro$  averaged over the subtropical region in different longitudinal sectors.

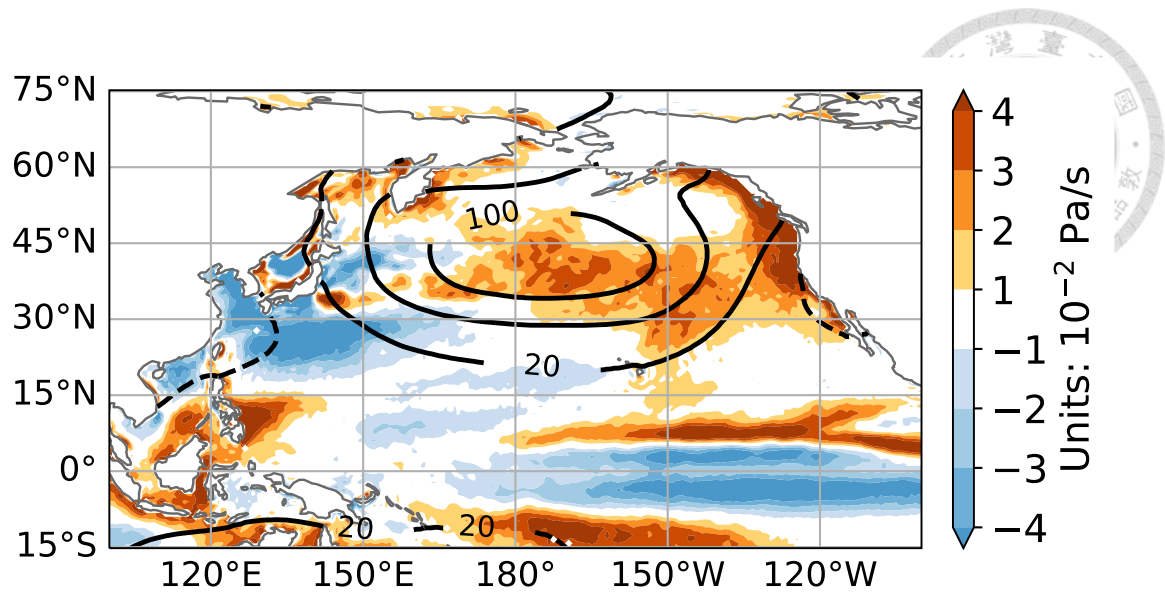


**Fig. 4.2** As in Fig. 1.1d, but for differences between April and January.

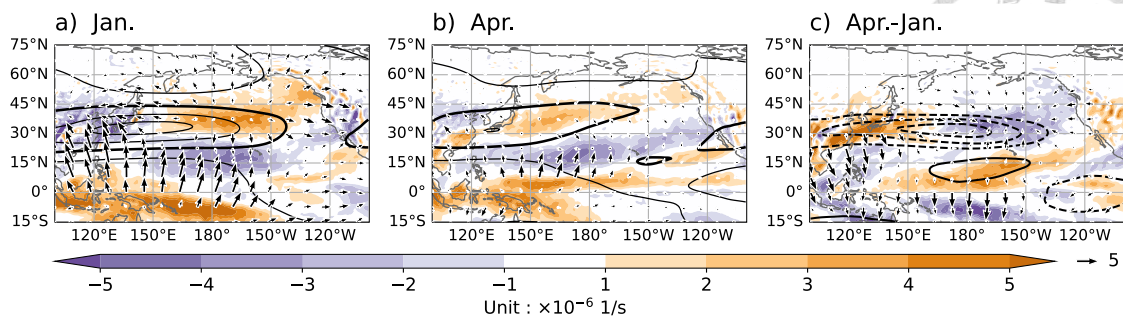


**Fig. 4.3** Climatology of 200 hPa divergence (shading), zonal wind (contour), and divergent wind (arrow) in (a) January, (b) April, and (c) their differences between April and January.

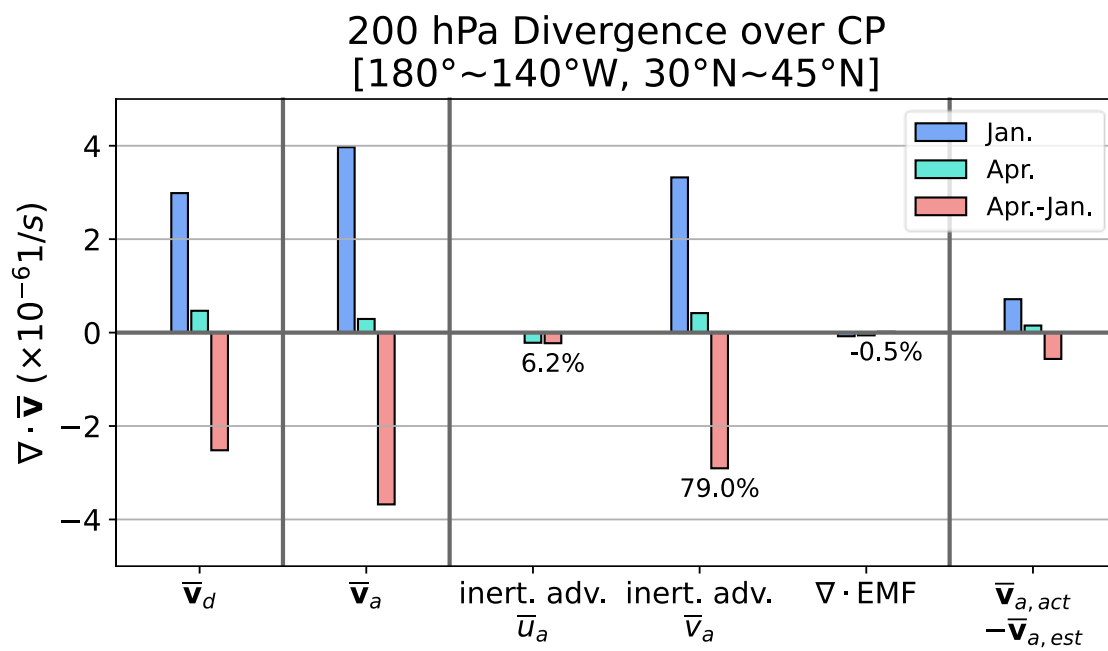


**Fig. 4.4** As in Fig. 3.4, but for the region over subtropical eastern central Pacific. The blue, green, and pink bars represent January, April, and the differences between April and January, respectively. The percentages below the bar are for the differences between months.

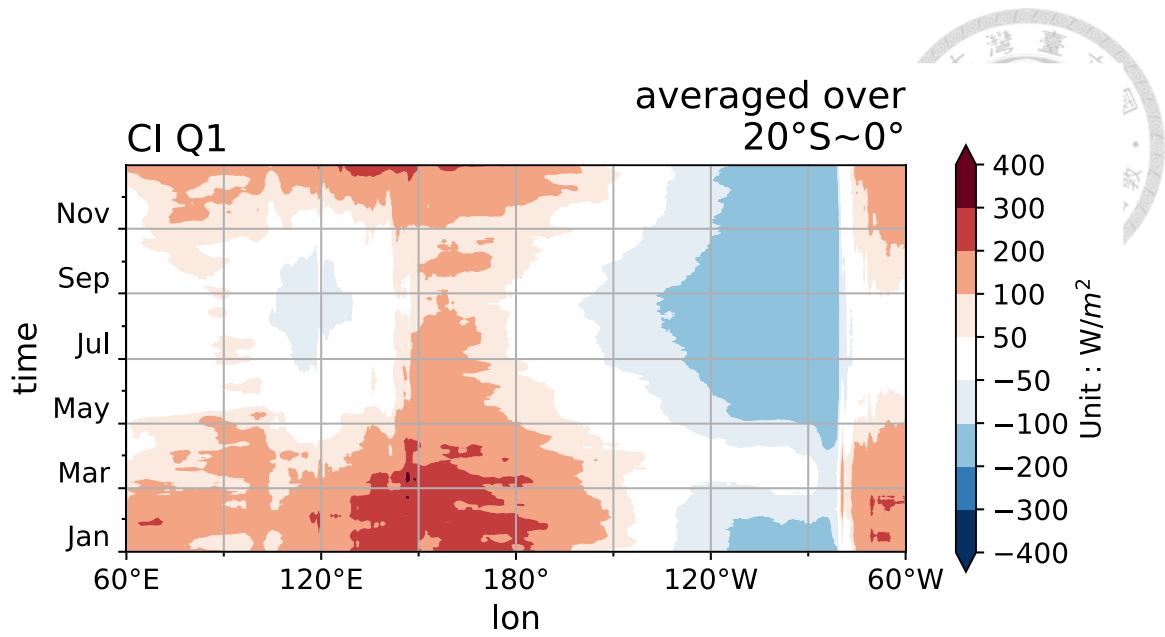


**Fig. 4.5** Hovmöller diagram of the column-integrated apparent heat source (Q1) meridionally averaged over  $20^{\circ}\text{S}\sim 0^{\circ}$ . The column-integrated values are mass-weighted vertical averaged Q1 from 70 hPa to surface. A  $\pm 5$ -days running mean is applied to the column-integrated Q1 field.

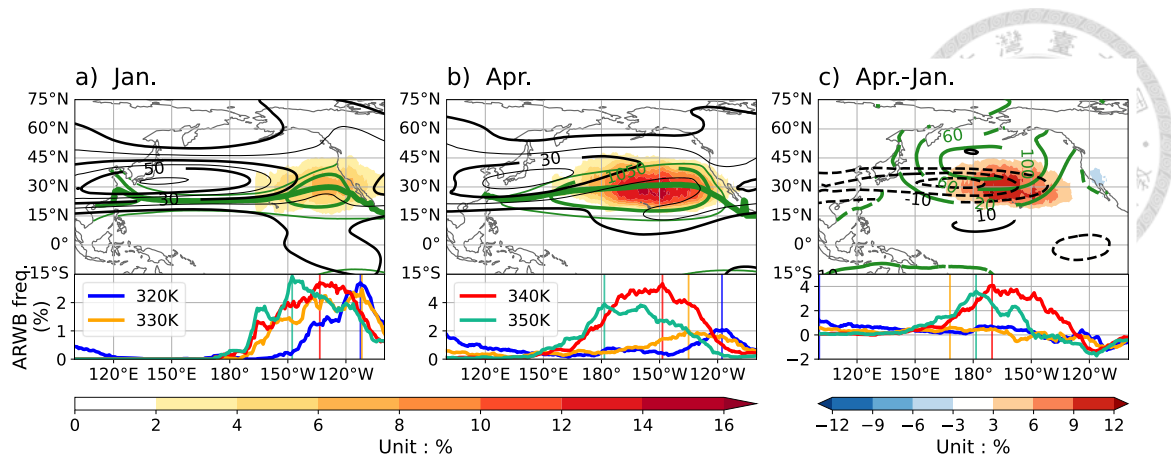


**Fig. 4.6** (upper) Climatology of anticyclonic Rossby wave breaking frequency (shading), zonal wind (black contour) on 340K isentrope and 900 hPa geopotential height (green contour) in (a) January, (b) April, and (c) their differences between April and January. The isentropic zonal wind is contoured in (a) and (b) in levels of 10, 20, 30, 40, 50, 70 m/s and in (c) with interval of 10 m/s. The contour intervals of 900 hPa geopotential height are 20 m in (a) and (b) and 40 m in (c). (lower) Climatology of meridionally averaged anticyclonic Rossby wave breaking frequency on each isentrope. The average is taken over  $0^{\circ}\sim 60^{\circ}\text{N}$ . The thin vertical lines are the longitude of maximum wave breaking frequency.



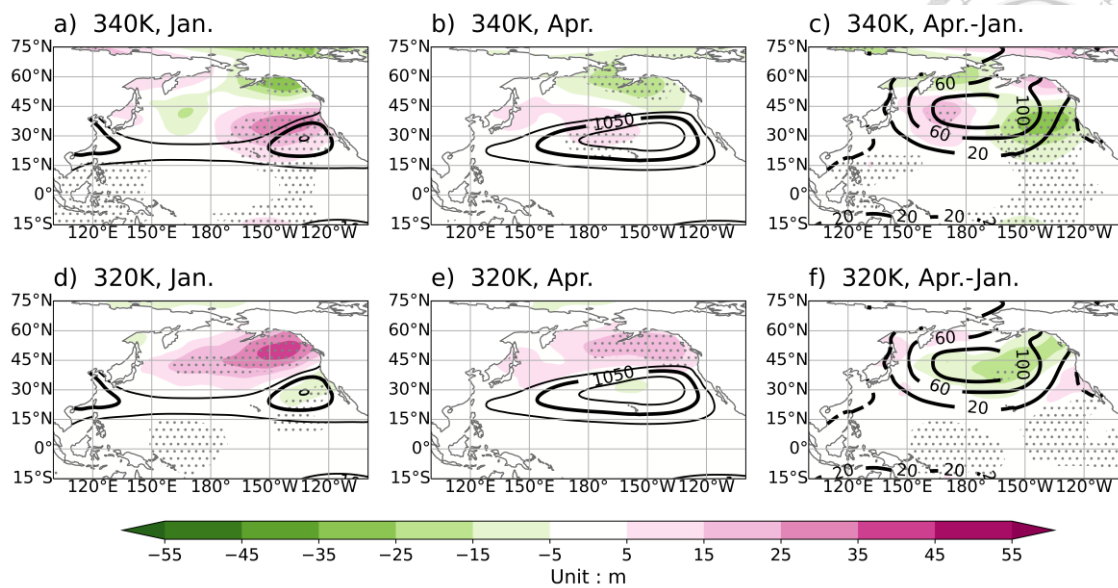


**Fig. 4.7** (upper) The composite of 900 hPa geopotential height anomalies on 340K anticyclonic Rossby wave breaking days (shading) and the climatology of geopotential height (contour) in (a) January, (b) April, and (c) their differences between April and January. The contour intervals of 900 hPa geopotential height are 20 m in (a) and (b) and 40 m in (c). The statistically significant ( $p=5\%$ ) anomalies are denoted by grey dots. (lower) As in the upper row, but for the composite of 320K anticyclonic Rossby wave breaking days.

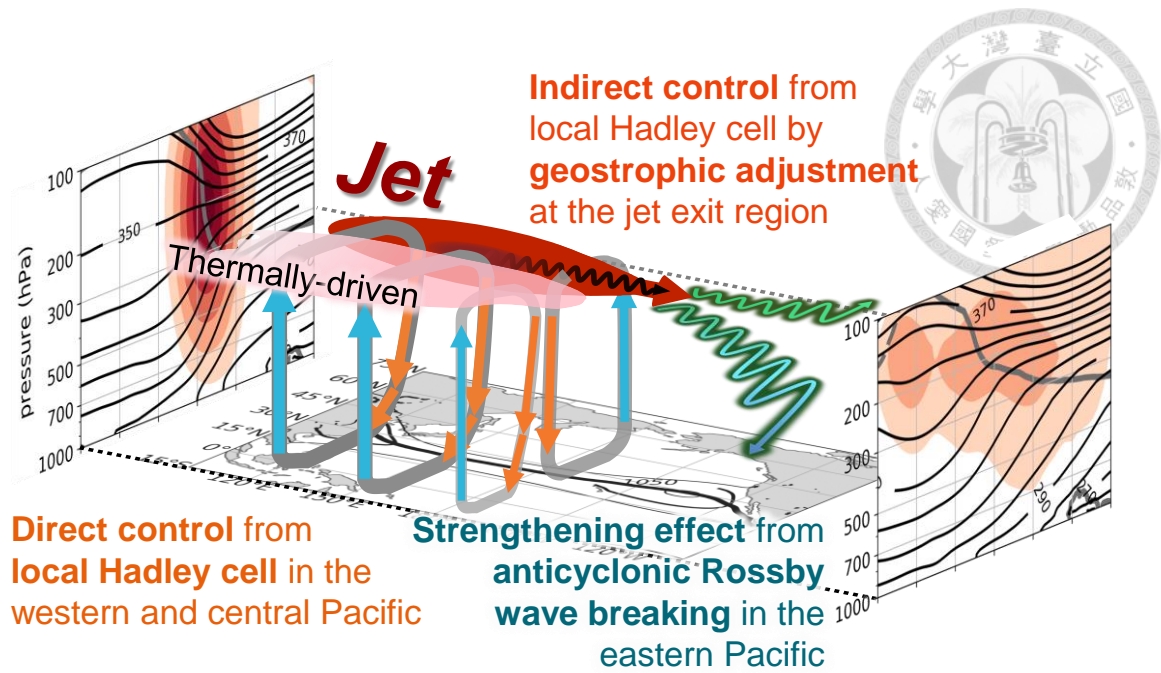


**Fig. 5.1** Summary schematics of the jet-mediated controlling factor of the North Pacific subtropical high in winter and spring. The figures on the left and right are the vertical profile of zonal wind (shading), isentropes (contour), and 2PVU isolines (grey line) in the central and eastern Pacific.